

Mock galaxy shape catalogues in the Subaru Hyper Suprime-Cam Survey

Masato Shirasaki¹★, Takashi Hamana¹, Masahiro Takada², Ryuichi Takahashi³,
and Hironao Miyatake^{2,4,5}

¹National Astronomical Observatory of Japan, Mitaka, Tokyo 181-8588, Japan

²Kavli Institute for the Physics and Mathematics of the Universe (WPI), The University of Tokyo Institutes for Advanced Study (UTIAS), The University of Tokyo, 5-1-5 Kashiwanoha, Kashiwa-shi, Chiba, 277-8583, Japan

³Faculty of Science and Technology, Hirosaki University, 3 Bunkyo-cho, Hirosaki, Aomori, 036-8561, Japan

⁴Institute for Advanced Research, Nagoya University, Nagoya 464-8601, Japan

⁵Division of Physics and Astrophysical Science, Graduate School of Science, Nagoya University, Nagoya 464-8602, Japan

ABSTRACT

We use the full-sky ray-tracing weak lensing simulations to generate 2268 mock catalogues for the Subaru Hyper Suprime-Cam (HSC) survey first-year shear catalogue. Our mock catalogues take into account various effects as in the real data: the survey footprints, inhomogeneous angular distribution of source galaxies, statistical uncertainties in photometric redshift (photo- z) estimate, variations in the lensing weight, and the statistical noise in galaxy shape measurements including both intrinsic shapes and the measurement errors. We then utilize our mock catalogues to evaluate statistical uncertainties expected in measurements of cosmic shear two-point correlations ξ_{\pm} with tomographic redshift information for the HSC survey. We develop a quasi-analytical formula for the Gaussian sample variance properly taking into account the number of source pairs in the survey footprints. The standard Gaussian formula significantly overestimates or underestimates the mock results by 50% level. We also show that different photo- z catalogues or the six disconnected fields, rather than a consecutive geometry, cause variations in the covariance by $\sim 5\%$. The mock catalogues enable us to study the chi-square distribution for ξ_{\pm} . We find the wider distribution than that naively expected for the distribution with the degrees-of-freedom of data vector used. Finally, we propose a method to include non-zero multiplicative bias in mock shape catalogue and show the non-zero multiplicative bias can change the effective shape noise in cosmic shear analyses. Our results suggest an importance of estimating an accurate form of the likelihood function (and therefore the covariance) for robust cosmological parameter inference from the precise measurements.

Key words: gravitational lensing: weak — cosmology: observations — method: numerical

1 INTRODUCTION

Weak gravitational lensing is one of the main subjects in modern cosmology to improve our understanding of the universe at low redshifts. Gravitational lensing analysis has a distinct advantage over other probes, enabling to observe total matter density distributions along a line of sight in an unbiased way, regardless of states of matter density. Hence, statistical analyses of gravitational lensing data can provide a complete map of large-scale structures in the universe and rich cosmological information printed in the lensing data will reveal the nature of dark matter (e.g. Ichiki et al. 2009; Markovic et al. 2011; Kamada et al. 2014) and the origin of cosmic acceleration (e.g. Weinberg et al. 2013; Shirasaki et al. 2017a). An attractive feature of weak lensing analyses leads to keen competition

among different groups. Ongoing scientific programs include the Kilo-Degree Survey (KiDS¹), the Dark Energy Survey (DES²), and the Subaru Hyper Suprime-Cam Survey (HSC³), while the Wide Field Infrared Survey Telescope (WFIRST⁴), the Large Synoptic Survey Telescope (LSST⁵), and Euclid⁶ will aim at measuring the gravitational lensing effect on distant galaxies with higher precision than the current surveys by covering a wider sky coverage and collecting fainter source galaxies.

As rich lensing data set becomes available and analysis method

¹ <http://kids.strw.leidenuniv.nl/index.php>

² <https://www.darkenergysurvey.org/>

³ <http://hsc.mtk.nao.ac.jp/ssp/>

⁴ <https://wfirst.gsfc.nasa.gov/>

⁵ <https://www.lsst.org/>

⁶ <http://sci.esa.int/euclid/>

★ E-mail: masato.shirasaki@nao.ac.jp

becomes diverse, robust estimation of statistical uncertainty in the analyses gains importance (e.g. Hartlap et al. 2007; Taylor et al. 2013; Friedrich et al. 2016; Sellentin & Heavens 2017; Friedrich & Eifler 2018) and a number of systematic effects must be addressed (Massey et al. 2013; Mandelbaum 2017). A possible approach to overcome these challenges is to carry out numerical simulations which capture the relevant gravitational physics for lensing analyses and create a mock catalogue of lensing data by including various observational effects with appropriate recipe.

Heymans et al. (2012) have utilized 185 independent realizations of CLONE catalogue (Harnois-Déraps et al. 2012) and produced the mock shape catalogues of the Canada-France-Hawaii Lensing Survey (CFHTLenS). The CFHTLenS mock catalogues have a high angular resolution of 0.2 arcmin but also suffer from small sky coverages. It is worth noting single CFHTLenS mock can cover 12.84 square degrees and the robust estimation of cosmic shear covariance is limited in the angular range of 0.5 – 40 arcmin. Hildebrandt et al. (2017) have improved the production of mock catalogues for first 450 squared degrees of KiDS (KiDS450) data compared to the case in CFHTLenS by increasing the simulation volume and the number of independent realizations (Harnois-Déraps & van Waerbeke 2015). The KiDS450 mock catalogues have been produced from 1025 independent set of N -body simulations with the box size of $505 h^{-1}$ Mpc and the sky coverage of each mock realization is set to be 100 squared degrees. (see Harnois-Déraps et al. 2018, for details). Note that either of CFHTLenS and KiDS450 mock catalogue is not designed to cover the survey footprint in a single realization.

Becker et al. (2016) have considered the mock catalogue production by performing ray-tracing simulation on a curved sky (Becker 2013) and the resulting mock catalogue for DES Science Verification (DES SV) data can cover whole survey footprint of DES SV data (139 squared degrees). Nevertheless, the number of independent mock catalogues is only 126 since the mock catalogues are based on single full-sky lensing simulation. Hence, direct covariance estimation from mock catalogues seems very challenging with DES SV mocks alone. The DES collaboration recently updated their weak lensing analyses with DES Year 1 (DES Y1) data (Troxel et al. 2018a). The fiducial pipeline to evaluate the statistical uncertainty of cosmological analyses with DES Y1 data relies on the analytic approach developed in Eifler et al. (2014); Krause & Eifler (2017); Krause et al. (2017). They validated their analytic approach by using mock catalogues of DES Y1 data, while the DES Y1 mock catalogue is based on log-normal simulation which is the approximated version of N -body simulation. It is uncertain if the approach developed in DES Y1 analyses works in other lensing surveys with a high source number density, such as the Subaru HSC (Mandelbaum et al. 2018a), since accurate modeling of non-linear gravitational growth becomes essential as source number density increases.

This paper presents a set of mock catalogues for the first data of Subaru HSC lensing survey, referred to as HSC S16A. The HSC S16A mock catalogues are based on 108 quasi-independent full-sky simulations (Takahashi et al. 2017). Making the best use of full-sky coverage, we extract six separated fields in HSC S16A survey footprint from a full-sky simulation multiple times. In the end, we produce 2268 realizations of HSC S16A mock catalogue with the same sky coverage as the actual shape catalogue. We apply the method in Shirasaki et al. (2017b) to the HSC S16A data when producing individual mock catalogues. Our pipeline in mock catalogue production refers both of simulated lensing data and observed galaxy images on object-by-object basis. Hence, our mock

catalogues have the exact same features appeared in the real catalogue, such as the angular position, the posterior distribution of photometric redshift, and the lensing weight of each source galaxy. According to the above features, our mock catalogues can be applied to any cosmic shear analyses with the HSC S16A shape catalogue and will be useful to evaluate the statistical uncertainty and validate the analysis pipeline. In this paper, we validate our mock catalogues by measuring two-point correlation functions of galaxy shapes ξ_{\pm} and comparing with the mock covariance of ξ_{\pm} and a theoretical prediction in detail. Note that the mock catalogs in this paper will be used in our forthcoming cosmological studies with HSC S16A, including cosmic shear analysis on real space (Hamana et al. in prep) and galaxy-galaxy lensing analysis (Miyatake et al. in prep).

This paper is organized as follows. In Section 2, we introduce the basics of gravitational lensing in galaxy imaging surveys and a theoretical framework to compute the expectation value of ξ_{\pm} and its statistical uncertainty. We then describe the HSC S16A shape catalogue which is used for cosmological analyses in first HSC data release in Section 3. The production procedure of the HSC S16A mock catalogues is summarized in Section 4. In Section 5, we compare the average ξ_{\pm} and the covariance of ξ_{\pm} at four different redshifts measured in 2268 mock catalogues with their theoretical predictions. Apart from detailed comparisons with mock results and analytic models, we also study the impact of field variance in the HSC S16A footprint and methodological difference in source redshift estimation on the mock covariance of ξ_{\pm} . In addition, we quantify the likelihood function of observed ξ_{\pm} in the HSC S16A analysis by using 2268 mock observations. Furthermore, we introduce a method to include non-zero multiplicative bias in our HSC S16A mock catalogues in an analysis-dependent way. We conclude this paper in Section 6.

2 WEAK GRAVITATIONAL LENSING

2.1 Basics

We first summarize the basics of gravitational lensing induced by large-scale structure. Weak gravitational lensing effect is usually characterized by the distortion of image of a source object by the following 2D matrix:

$$A_{ij} = \frac{\partial \beta^i}{\partial \theta^j} \equiv \begin{pmatrix} 1 - \kappa - \gamma_1 & -\gamma_2 \\ -\gamma_2 & 1 - \kappa + \gamma_1 \end{pmatrix}, \quad (1)$$

where θ represents the observed position of a source object, β is the true position, κ is the convergence, and γ is the shear. In the weak lensing regime (i.e., $\kappa, \gamma \ll 1$), each component of A_{ij} can be related to the second derivative of the gravitational potential Φ (Bartelmann & Schneider 2001). Using the Poisson equation and the Born approximation, one can express the weak lensing convergence field as the weighted integral of matter overdensity field $\delta_m(\mathbf{x})$:

$$\kappa(\theta) = \int_0^{\chi_H} d\chi q(\chi) \delta_m(\chi, r(\chi)\theta), \quad (2)$$

where χ is the comoving distance, χ_H is the comoving distance up to $z \rightarrow \infty$ and $q(\chi)$ is called lensing kernel. For a given redshift distribution of source galaxies, the lensing kernel is expressed as

$$q(\chi) = \frac{3}{2} \left(\frac{H_0}{c} \right)^2 \Omega_{m0} \frac{r(\chi)}{a(\chi)} \int_{\chi}^{\chi_H} d\chi' p(\chi') \frac{r(\chi' - \chi)}{r(\chi')}, \quad (3)$$

where $r(\chi)$ is the angular diameter distance and $p(\chi)$ represents the redshift distribution of source galaxies normalized to $\int_0^{\chi_H} d\chi p(\chi) = 1$.

Power spectrum is a relevant statistical quantity in two-point correlation analysis in weak lensing surveys. For two source galaxy populations with different $p(\chi)$, it is defined as

$$\langle \tilde{\kappa}_a(\ell_1) \tilde{\kappa}_b(\ell_2) \rangle \equiv (2\pi)^2 \delta^{(2)}(\ell_1 - \ell_2) P_{\kappa,ab}(\ell), \quad (4)$$

where $\tilde{\kappa}$ is the Fourier counterpart of convergence, the indices a and b represent any two source populations, $\delta^{(n)}(\mathbf{x})$ is the Dirac delta function in n -dimensional space, and $P_{\kappa,ab}$ is the convergence power spectrum. Under the Limber approximation (Limber 1954), we can express the power spectrum as

$$P_{\kappa,ab}(\ell) = \int_0^{\chi_H} \frac{d\chi}{r^2(\chi)} q_a(\chi) q_b(\chi) P_m\left(\frac{\ell}{r(\chi)}, z(\chi)\right), \quad (5)$$

where q_a is the lensing kernel for the source catalogue “ a ” and it is defined as in Eq. (3). In Eq. (5), $P_m(k, z)$ represents the non-linear matter power spectrum for wavelength of k at redshift z .

2.2 Cosmic shear

The observed galaxy shape is commonly used as an estimator of weak-lensing shear γ . In this paper, we use distortion of galaxy as an estimator, and denote it as ϵ . The definition of ϵ is provided in Eq. (19). In wide-area galaxy imaging surveys, a correlation function method is most conventionally used for cosmological analysis (e.g. Hildebrandt et al. 2017, Köhlinger et al. 2017, van Uitert et al. 2018, Troxel et al. 2018a, Hikage et al. 2018 and see Köhlinger et al. 2017, van Uitert et al. 2018 for some exceptions). One can estimate the correlation function by cross-correlating lensing shear of two galaxies as a function of separation angles:

$$\xi_{\pm}(\theta) = \langle \gamma_t(\theta_1) \gamma_t(\theta_2) \pm \gamma_{\times}(\theta_1) \gamma_{\times}(\theta_2) \rangle_{|\theta_1 - \theta_2| = \theta}, \quad (6)$$

where the average is done over all pairs of galaxies separated by a fixed separation angle, θ in the above case. In Eq. (6), we define the tangential and cross components of $\gamma = \gamma_1 + i\gamma_2$ as

$$\gamma_t \equiv -Re \left[\gamma e^{-2i\phi} \right], \quad \gamma_{\times} \equiv -Im \left[\gamma e^{-2i\phi} \right], \quad (7)$$

where ϕ represents the polar angle of separation vector between two galaxies from the 1st axis, θ .

In the absence of residual systematic errors in galaxy shape measurement, the expectation value of ξ_{\pm} for two source populations is given, e.g. in Bartelmann & Schneider (2001), by

$$\xi_{\pm,ab}(\theta) = \int_0^{\infty} \frac{\ell d\ell}{2\pi} P_{\kappa,ab}(\ell) J_{0,4}(\ell\theta), \quad (8)$$

where $J_{0,4}(x)$ are the zero-th and fourth order Bessel functions of the first kind, respectively. The zero-th order Bessel function should be adopted for ξ_+ , while the fourth one is for ξ_- .

Schneider et al. (2002) showed that the two point correlation functions of lensing shear are estimated in an unbiased way by averaging distortions over pairs of galaxies. In practice, the estimator $\hat{\xi}_{\pm,ab}$ is calculated by

$$\hat{\xi}_{\pm,ab}(\theta) = \frac{1}{(2\mathcal{R}^{(a)})(2\mathcal{R}^{(b)})} \frac{1}{N_p^{ab}(\theta)} \sum_{ij} w_i^{(a)} w_j^{(b)} \Delta_{\theta}(\theta_i - \theta_j) \times \left(\epsilon_i^{(a)}(\theta_i) \epsilon_j^{(b)}(\theta_j) \pm \epsilon_{\times}^{(a)}(\theta_i) \epsilon_{\times}^{(b)}(\theta_j) \right), \quad (9)$$

$$N_p^{ab}(\theta) = \sum_{ij} w_i^{(a)} w_j^{(b)} \Delta_{\theta}(\theta_i - \theta_j), \quad (10)$$

where $w_i^{(a)}$ is weight related to shape measurement of i -th galaxy in

catalogue “ a ”, $\mathcal{R}^{(a)}$ is the responsivity⁷ for catalogue “ a ”, $\Delta_{\theta}(\phi) = 1$ for $\theta - \Delta\theta/2 \leq \phi \leq \theta + \Delta\theta/2$ and zero otherwise. The expectation value of this estimator is evaluated by an ensemble average of the shear field γ and it is known to be unbiased, i.e. $\langle \hat{\xi}_{\pm,ab}(\theta) \rangle = \xi_{\pm,ab}(\theta)$.

2.3 Statistical uncertainties of cosmic shear correlation functions

We then consider statistical uncertainties of cosmic shear correlation functions defined in Section 2.2. For our observables, the covariance matrix is commonly adopted for an evaluation of the statistical uncertainties. The covariance matrix of two-point correlation function, denoted as C , can be decomposed into three parts:

$$C = C_G + C_{\text{cNG}} + C_{\text{SSC}}, \quad (11)$$

where C_G represents the Gaussian error, and other two terms denote the non-Gaussian errors arising from the four-point correlations of matter field in large-scale structure. The contribution C_{cNG} arises from the four-point correlation within a given survey area (Cooray & Hu 2001; Takada & Jain 2009), while the term C_{SSC} arises from correlations between sub-survey (observable) modes and super-survey (unobservable) modes comparable with or greater than the size of a survey window (SSC stands for Super Sample Covariance; Takada & Hu 2013).

2.3.1 Gaussian covariance

Following Joachimi et al. (2008), we use a formula for the Gaussian covariance expressed in terms of the convergence power spectrum:

$$\text{Cov}_G [\hat{\xi}_{X,ab}(\theta_1), \hat{\xi}_{Y,cd}(\theta_2)] = \frac{1}{\Omega_s} \int_0^{\infty} \frac{\ell d\ell}{2\pi} J_x(\ell\theta_1) J_y(\ell\theta_2) \times \left(P_{\kappa,ac}^{\text{obs}}(\ell) P_{\kappa,bd}^{\text{obs}}(\ell) + P_{\kappa,ad}^{\text{obs}}(\ell) P_{\kappa,bc}^{\text{obs}}(\ell) \right), \quad (12)$$

where Ω_s is the survey area and we use the notation of $J_x = J_0$ for $\xi_X = \xi_+$ and $J_x = J_4$ for $\xi_X = \xi_-$ and so on. In the above, $P_{\kappa,ab}^{\text{obs}}(\ell)$ represents the *observed* convergence power spectrum which includes a contribution of intrinsic shape noise of source galaxies. It is given by

$$P_{\kappa,ab}^{\text{obs}}(\ell) = P_{\kappa,ab}(\ell) + \frac{1}{\bar{n}_{s,a}} \left(\frac{\sigma_{\epsilon,a}}{2\mathcal{R}^{(a)}} \right)^2 \delta_{ab}^K, \quad (13)$$

where δ_{ab}^K is the Kronecker delta function, $\sigma_{\epsilon,a}$ and $\bar{n}_{s,a}$ are the rms of intrinsic galaxy distortions per component and the mean source number density in catalogue “ a ”, respectively. Note $\sigma_{\epsilon}^2 = \epsilon_{\text{rms}}^2 + \sigma_e^2$ in terms of notations we introduce below: the shape noise arises from a sum of the “intrinsic” distortion and the measurement error. On large scales comparable to the size of a survey window, the Gaussian prediction of Eq. (12) will be inaccurate because Eq. (12) ignores the boundary effect of survey window. This finite area effect will be important for the HSCS16A data with sky coverage of ~ 100 squared degrees. Sato et al. (2011) developed the method to correct for the finite area effect of Gaussian covariance based on the direct pair counting of observed galaxies. We extend their method to make

⁷ The factor of $2\mathcal{R}$ is needed for conversion of distortion to lensing shear γ_t , due to the definition of distortion used in this paper (see Eq. (19) in Bernstein & Jarvis 2002).

it valid for tomographic analyses in Appendix A. A similar investigation of the impact of survey geometry on covariance estimation is found in Troxel et al. (2018b). It is worth noting that this study focuses on the case where the shape noise is less important, while Troxel et al. (2018b) mainly studied the effect of survey geometry on shape noise covariances.

2.3.2 Non-Gaussian covariance

The non-Gaussian covariance term of Eq. (9) is expressed as the sum of following two contributions:

$$\text{Cov}_{\text{cNG}}[\hat{\xi}_{X,ab}(\theta_1), \hat{\xi}_{Y,cd}(\theta_2)] = \frac{1}{\Omega_s} \int \frac{d^2\ell'}{(2\pi)^2} \int \frac{d^2\ell}{(2\pi)^2} \times J_x(\ell\theta_1) J_y(\ell'\theta_2) T_{\kappa,abcd}^{\text{cNG}}(\ell, -\ell, \ell', -\ell'), \quad (14)$$

$$\text{Cov}_{\text{SSC}}[\hat{\xi}_{X,ab}(\theta_1), \hat{\xi}_{Y,cd}(\theta_2)] = \int_0^\infty \frac{\ell' d\ell'}{2\pi} \int_0^\infty \frac{\ell d\ell}{2\pi} \times J_x(\ell\theta_1) J_y(\ell'\theta_2) T_{\kappa,abcd}^{\text{SSC}}(\ell, \ell', \Omega_s), \quad (15)$$

where T_κ denotes the convergence trispectrum describing the four-point correlation function in Fourier space. Using the Limber approximation, the connected trispectrum $T_{\kappa,abcd}^{\text{cNG}}$ in Eq. (14) can be computed (e.g., Cooray & Hu 2001; Takada & Jain 2009) as

$$T_{\kappa,abcd}^{\text{cNG}}(\ell_1, \ell_2, \ell_3, \ell_4) = \int_0^{\chi_H} \frac{d\chi}{r^6(\chi)} q_a(\chi) q_b(\chi) q_c(\chi) q_d(\chi) \times T_m\left(\frac{\ell_1}{r(\chi)}, \frac{\ell_2}{r(\chi)}, \frac{\ell_3}{r(\chi)}, \frac{\ell_4}{r(\chi)}, z(\chi)\right), \quad (16)$$

where $\ell_1 + \ell_2 + \ell_3 + \ell_4 = 0$ and T_m is the trispectrum of cosmic matter density field. On the other hand, the SSC trispectrum $T_{\kappa,abcd}^{\text{SSC}}$ can be expressed in Takada & Hu (2013) as

$$T_{\kappa,abcd}^{\text{SSC}}(\ell_1, \ell_2, \Omega_s) = \int_0^{\chi_H} \frac{d\chi}{r^6(\chi)} q_a(\chi) q_b(\chi) q_c(\chi) q_d(\chi) \times \frac{\partial P_m(k_1, z)}{\partial \delta_{\text{bg}}} \frac{\partial P_m(k_2, z)}{\partial \delta_{\text{bg}}} \sigma_w^2(z; \Omega_s), \quad (17)$$

where

$$\sigma_w^2(z; \Omega_s) \equiv \frac{1}{\Omega_s^2} \int \frac{d^2\ell}{(2\pi)^2} P_{m,L}(\ell/\chi(z), z) |\bar{W}(\ell)|^2, \quad (18)$$

and $k_i = \ell_i/\chi$, $P_{m,L}$ is the linear matter power spectrum, and \bar{W} is the Fourier transform of survey window function. Note we define the window function so that $\Omega_s = \int d^2\theta W(\theta)$. In Eq. (17), $\partial P_m(k, z)/\partial \delta_{\text{bg}}$ describes the response of power spectrum to a fluctuation in background density δ_{bg} . The SSC trispectrum arises from the four point correlation with squeezed quadrilaterals including a shared infinite wavelength mode.

3 SUBARU HYPER SUPRIME-CAM SURVEY

Hyper Suprime-Cam (HSC) is a wide-field imaging camera on the prime focus of the 8.2-meter Subaru telescope (Miyazaki et al. 2015; Aihara et al. 2018; Komiya et al. 2018; Furusawa et al. 2018; Miyazaki et al. 2018). Among three layers in the HSC survey, the Wide layer will cover 1400 deg² in five broad photometric bands (*grizy*) over 5-6 years, with excellent image quality of sub-arcsec seeing. In this paper, we use a catalogue of galaxy shapes that has been generated for cosmological weak lensing analysis in the first year data release. The details of galaxy shape measurements and catalogue information are found in Mandelbaum et al. (2018a).

In brief, the HSC S16A galaxy shape catalogue is based on the HSC Wide data taken from March 2014 to April 2016 with about 90 nights. We apply a number of cuts to construct a secure shape catalogue for weak lensing analysis (see Mandelbaum et al. 2018a, for more details). The selection criteria include data selection with approximately full depth in all the 5 filters, a conservative magnitude cut of $i < 24.5$, removal of galaxies with PSF modeling failures and those located in the disconnected regions. The sky around bright stars are masked (Coupon et al. 2018). As a result, the HSC S16A weak lensing shear catalogue covers 136.9 deg² that consists of 6 disjoint patches: XMM, GAMA09H, GAMA15H, HECTOMAP, VVDS, and WIDE12H. In the HSC S16A shape catalogue, the shapes of galaxies are estimated on the *i*-band coadded images using the re-Gaussianization PSF correction method (Hirata & Seljak 2003). This method has been applied to the Sloan Digital Sky Survey data, from which the systematics of the method are well understood (Mandelbaum et al. 2005, 2013). In the method, the distortion of a galaxy image is defined as

$$\epsilon = (\epsilon_1, \epsilon_2) = \frac{1 - (b/a)^2}{1 + (b/a)^2} (\cos 2\phi, \sin 2\phi), \quad (19)$$

where b/a is the minor-to-major axis ratio and ϕ is the position angle of the major axis with respect to the equatorial coordinate system. The shear of each galaxy, $\gamma^{(\text{obs})}$, is estimated from the measured distortion ϵ as follows:

$$\gamma^{(\text{obs})} = \frac{1}{1 + \langle m \rangle} \left(\frac{\epsilon}{2\mathcal{R}} - c \right), \quad (20)$$

where \mathcal{R} represents the response of our distortion definition to a small shear (Bernstein & Jarvis 2002) given by

$$\mathcal{R} = 1 - \langle \epsilon_{\text{rms}}^2 \rangle, \quad (21)$$

where ϵ_{rms} is the intrinsic root mean square (RMS) distortion per component. $\langle \cdot \rangle$ means the weighted average with galaxy weight w which is defined as the inverse variance of the shape noise

$$w = (\sigma_e^2 + \epsilon_{\text{rms}}^2)^{-1}, \quad (22)$$

where σ_e represents the shape measurement error for each galaxy. The values m and c represent the multiplicative and additive biases in galaxy shapes. Mandelbaum et al. (2018b) estimated both shape errors and biases on object-by-object basis by using image simulations. We fully utilize the information of shape errors to construct mock catalogues of HSC S16A galaxy shapes (see Section 4.2 for details). In each patch, the survey windows is defined such that 1) the number of visits within HEALPIX pixels with NSIDE=1024 to be $(g, r, i, z, y) \geq (4, 4, 4, 6, 6)$ and the *i*-band limiting magnitude to be greater than 25.6, 2) the PSF modeling is good enough to meet our requirements on PSF model size residuals and residual shear correlation functions, 3) there are no disconnected HEALPIX pixels after the cut 1) and 2), and 4) the galaxies do not lie within the bright object masks. For details of defining these masks, see Mandelbaum et al. (2018a).

The redshift distribution of source galaxies is estimated from the HSC five broadband photometry. Tanaka et al. (2018) measured photometric redshifts (photo-*z*'s) of galaxies in the HSC survey by using several different codes. Among them, we choose the photo-*z* with a machine-learning code based on self-organizing map (MLZ) as a baseline⁸. To study the impact of photo-*z* estimation with different methods, we consider three additional photo-*z*'s estimated from

⁸ This is simply because the number of available photo-*z* estimates is found to be largest in the photo-*z* catalogue based on MLZ.

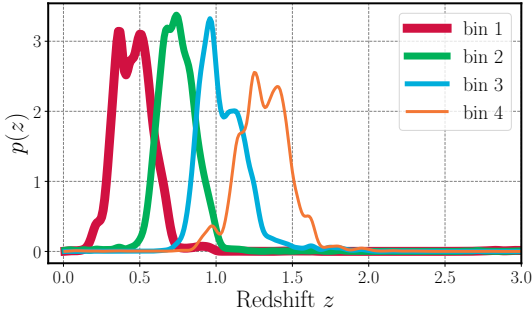


Figure 1. The stacked posterior redshift distributions of source galaxies in four tomographic redshift bins, which are used for the cosmic shear tomography analysis of HSC S16A data. Here we adopt the MLZ catalogue of the photometric redshifts in Tanaka et al. (2018) as a default catalogue used in the HSC mock catalogues.

a classical template-fitting code (Mizuki), a neural network code using the CModel photometry (ephor), and a hybrid code combining machine learning with template fitting (frankenZ). When performing tomographic cosmic shear analyses, we divide the source galaxies into 4 subsamples by their *best* estimates (see Tanaka et al. 2018) of the photo- z 's (z^{best}) in the redshift range from 0.3 to 1.5 as done in cosmic shear power spectrum analysis in the HSC S16A data (Hikage et al. 2018). The redshift range of each tomographic bin is set to be (0.3, 0.6), (0.6, 0.9), (0.9, 1.2), and (1.2, 1.5) for the binning number from 1 to 4. Figure 1 shows the stacked posterior distribution of photo- z of source galaxies in four different tomographic bins.

4 SIMULATIONS

4.1 Full-sky simulation

In order to construct the mock catalogues for weak lensing analyses in HSC, we utilize a large set of weak gravitational lensing simulations with all sky coverage. Here we briefly describe full-sky lensing catalogues⁹, while the details of these catalogues are found in Takahashi et al. (2017) (also see Shirasaki et al. 2017b). In Takahashi et al. (2017), the authors performed a set of N -body simulations with 2048^3 particles in cosmological volumes and used them to construct lensing and halo catalogues. They adopted the standard Λ CDM cosmology that is consistent with the WMAP cosmology (Hinshaw et al. 2013). The cosmological parameters are the CDM density parameter $\Omega_{\text{cdm}} = 0.233$, the baryon density $\Omega_{\text{b}} = 0.046$, the matter density $\Omega_{\text{m}} = \Omega_{\text{cdm}} + \Omega_{\text{b}} = 0.279$, the cosmological constant $\Omega_{\Lambda} = 0.721$, the Hubble parameter $h = 0.7$, the amplitude of density fluctuations $\sigma_8 = 0.82$, and the spectral index $n_s = 0.97$. In the following, we use 108 full-sky realizations in Takahashi et al. (2017).

Full-sky weak gravitational lensing simulations have been performed with the standard multiple lens-plane algorithm (e.g. Hamana & Mellier 2001; Becker 2013; Shirasaki et al. 2015). In this simulation, one can take into account the light-ray deflection on the celestial sphere by using the projected matter density field given

in the format of spherical shell (see, e.g. Fosalba et al. 2008, for the similar approach). The simulations used the projected matter fields in 38 shells in total, each of which was computed by projecting N -body simulation realization over a radial width of $150 h^{-1}$ Mpc, in order to make the light cone covering a cosmological volume up to $z = 5.3$. As a result, the lensing simulations consist of shear field at 38 different source redshifts with angular resolution of 0.43 arcmin. Each simulation data is given in the HEALPix format (Górski et al. 2005). The radial depth between nearest source redshifts is set to be $150 h^{-1}$ Mpc in comoving distance, corresponding to the redshift interval of 0.05 – 0.1 for $z \lesssim 1$.

4.2 Mock catalogues

We here describe the details of creating the mock shape catalogues in HSC S16A from 108 full-sky lensing simulations. To do this, we follow the approach developed in Shirasaki et al. (2017b) (also see Shirasaki & Yoshida 2014).

In our mock catalogues, we incorporate the full-sky simulations with observed photometric redshift and angular position of real galaxies. Provided that real catalogue of source galaxies, where each galaxy contains information on the position (RA and dec), shape, redshift and the lensing weight, the procedures in production of mock catalogues consists of five steps as follows:

- (i) Assign hypothetical RA and dec of survey window in the full-sky realization.
- (ii) Populate each source galaxy into one realization of the light-cone simulations according to its original angular position and redshift.
- (iii) Randomly rotate distortion of each source galaxy to erase the real lensing signal.
- (iv) Simulate the lensing distortion effect on each source galaxy by adding the lensing contribution at each foreground lens plane
- (v) Repeat the steps (ii) – (iv) for all the source galaxies

We then summarize some additional treatments to take into account the specific features in HSC on step-by-step basis.

Step (i) We pay a special attention to the positional relationship among HSC S16A regions. From a single full-sky simulation, we decide to make 21 mock shear catalogues by choosing the desired sky coverage of about 170 squared degrees which is the area when not taking into account masked regions and other cuts. Since 6 fields of HSC S16A are separated from each other, we define 21 different rotations on spherical coordinate so as to preserve the positional relationship among the HSC S16A fields. Figure 2 demonstrates the rotation of two HSC fields named as GAMA09H and GAMA15H. We set these rotations so that we do not use the same locations on full sky as possible. We found the area fraction of overlapped regions is about 2% over 21 rotations. Note that we properly modify the simulated lensing field by taking into account the change of locally orthogonal coordinate system under a given rotation. Since 108 full-sky lensing simulations are available, we have $108 \times 21 = 2268$ realizations of each region of HSC S16A in total. Under the rotation, we also keep the angular coordinates of individual source galaxies in the survey window. Hence, the source galaxies in our mock have exactly same angular information as in the real catalogue.

Step (ii) When injecting each galaxy taken from the real HSC source catalogue into the light-cone simulation, we use the nearest pixel in the source plane at the nearest redshift, to those of the galaxy.

⁹ The full-sky light-cone simulation data are freely available for download at http://cosmo.phys.hirosaki-u.ac.jp/takahashi/allsky_raytracing/.

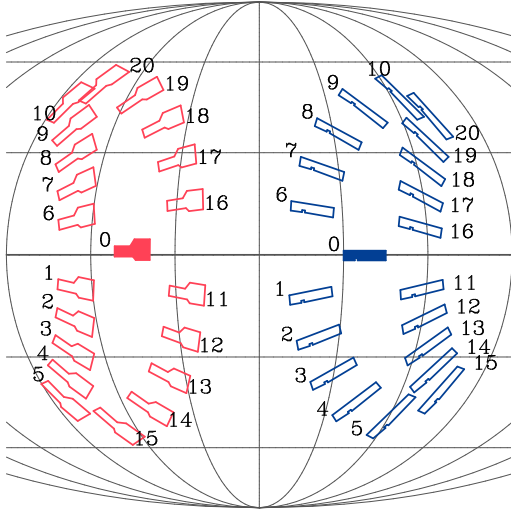


Figure 2. Distributions of the HSC fields in our full-sky mock catalogues. For each full-sky simulation, we take 21 realizations of the six distinct HSC fields. Here, for illustration purpose, we show only the two fields among six, the GAMA09 and GAMA15H fields, by red and blue regions. The filled regions show the locations without rotation, while the blank regions are their locations taken after rotations that are determined so that the different realizations are not overlapped with each other (see text for details). The indices ranging from 0 to 20 represent each of the 21 realizations. Their relative locations of GAMA09 and GAMA15H in each realization are taken the same as those of the real HSC data.

In doing this we use a point redshift estimate of each galaxy, taken from a random sampling of the posterior distribution of MLZ photometric redshift estimate for the galaxy. It is worth noting that we randomly generate redshift distributions of source galaxies when making a different realization of the mock catalogues. Thus, our mock catalogues include effects of source galaxy properties (e.g., magnitudes, distortions and spatial variations in the number densities), statistical uncertainties in photometric redshifts and the survey geometry. Although we use MLZ photometric redshift estimate as our fiducial choice, we also examine how the results are changed by using different photo- z catalogues, `ephor`, `mizuki`, and `frankenz`. We have created 2268 realizations for MLZ, while we have generated 210 realizations for `ephor`, `mizuki`, and `frankenz`.

Step (iii) Rotating the observed distortion of each galaxy allows to eliminate real lensing distortions and intrinsic alignment signal existing in galaxy images. Assuming the amplitude in observed distortion is mainly determined by the intrinsic shape, we can use this rotated distortion as a proxy of the intrinsic shape. Nevertheless, the observed distortion contains an additional scatter due to the shape measurement error. Following [Oguri et al. \(2018\)](#) we simulate an “observed” distortion of each galaxy taking into account both the intrinsic shape and measurement error. We first rotate the distortion of individual galaxies ϵ^{obs} and obtain the rotated distortion as $\epsilon^{\text{ran}} = \epsilon^{\text{obs}} e^{i\phi}$, where ϕ is a random number between 0 and 2π . Here we need to distinguish the intrinsic distortion from the measurement error because the shear responsivity depends only on the intrinsic shape noise (rms). We thus model the intrinsic shape ϵ^{int} and measurement error ϵ^{mea} from the following random generations:

$$\epsilon^{\text{int}} = \left(\frac{\epsilon_{\text{rms}}}{\sqrt{\epsilon_{\text{rms}}^2 + \sigma_e^2}} \right) \epsilon^{\text{ran}}, \quad \epsilon^{\text{mea}} = N_1 + i N_2, \quad (23)$$

where N_i is a random number drawn from a normal distribution with a standard deviation of σ_e . In the HSC shape catalogue, ϵ_{rms} (parameter `ishape_hsm_regauss_derived_rms_e`) and σ_e (parameter `ishape_hsm_regauss_derived_sigma_e`) are provided on object-by-object basis.

Step (iv) We then obtain the mock ellipticity ϵ^{mock} ([Miralda-Escude 1991](#); [Bernstein & Jarvis 2002](#)):

$$\epsilon_1^{\text{mock}} = \frac{\epsilon_1^{\text{int}} + \delta_1 + (\delta_2/\delta^2)[1 - (1 - \delta^2)^{1/2}](\delta_1\epsilon_{\text{int},2} - \delta_2\epsilon_1^{\text{int}})}{1 + \delta \cdot \epsilon^{\text{int}}} + \epsilon_1^{\text{mea}}, \quad (24)$$

$$\epsilon_2^{\text{mock}} = \frac{\epsilon_2^{\text{int}} + \delta_2 + (\delta_1/\delta^2)[1 - (1 - \delta^2)^{1/2}](\delta_2\epsilon_{\text{int},1} - \delta_1\epsilon_2^{\text{int}})}{1 + \delta \cdot \epsilon^{\text{int}}} + \epsilon_2^{\text{mea}}, \quad (25)$$

where $\delta \equiv 2(1 - \kappa)\gamma / [(1 - \kappa)^2 + \gamma^2]$ and κ and γ are simulated lensing effects at the galaxy position, taken from the light-cone simulation. Note $\delta \approx 2\gamma$ in the weak lensing regime and we ignore any multiplicative and additive biases in mock catalogues in Eqs. (24) and (25). Nevertheless, one can include multiplicative and additive biases in our catalogues if needed, since our mock catalogues share the same object ID with the real catalogue. Except for Section 5.6, we adopt Eqs. (24) and (25) for simplicity. We summarize the impact of non-zero multiplicative bias on the covariance of cosmic shear correlation function in Section 5.6.

5 RESULTS

5.1 Comparison with a theoretical model

In this section, we compare the statistical property of clustering observables obtained from our mock catalogues with its theoretical prediction in detail.

5.1.1 Cosmic shear

We validate the cosmic shear mock catalogues by comparing the cosmic shear correlation functions measured from the mocks with the theoretical expectation (Eq. 8). Figure 3 shows the averaged ξ_{\pm} from our 2268 realizations compared with the expectations. In this figure, we work with four different tomographic bins in source redshift selection as shown in Figure 1. For simplicity, we consider the auto correlation functions of ξ_{\pm} at single tomographic bin, i.e. $q_a = q_b$ in Eq. (5). Different colored points show the averaged ξ_{\pm} , while the lines represent the respective theoretical predictions that are computed using the fitting formula of non-linear matter power spectrum in [Takahashi et al. \(2012\)](#). When measuring the correlation function in our mock catalogues, we use the public code `Athena`¹⁰ ([Kilbinger et al. 2014](#)) and perform the logarithmic binning in the range of $0.281 < \theta$ [arcmin] < 354 with 31 bins. We use the source galaxies in all of HSC S16A fields in Figure 3. When comparing the averaged ξ_{\pm} with its expectation, we properly include the selection bias m_{sel} due to cuts in the resolution factor and the responsivity correction due to the intrinsic distortion variations as a function of redshift in the theoretical model (see Section 5.7 [Hikage et al. 2018](#), for details).

First of all, the estimation of average ξ in the mock catalogue should be reliable at $\theta \gtrsim 1$ arcmin for ξ_+ and $\theta \gtrsim 10$ arcmin for

¹⁰ <http://www.cosmostat.org/software/athena>

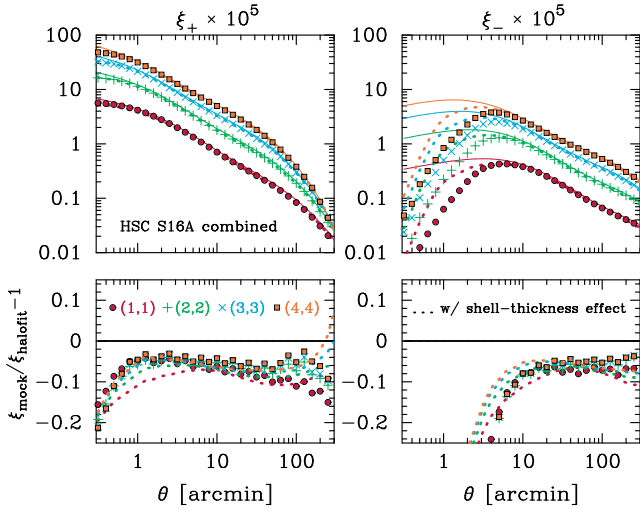


Figure 3. Comparison of the analytical model predictions with those measured from the HSC mock catalogues for the cosmic shear two-point correlation functions in four tomographic redshift bins as shown in Fig. 1. In the upper panels, the colored points show the averages of 2268 mock realizations, while the solid lines are the analytical predictions computed using the fitting formula of nonlinear matter power spectrum (Takahashi et al. 2012). The fractional differences are shown in the lower panels. The left and right plots are the results for ξ_+ and ξ_- , respectively. The dashed lines in each panel show the theoretical predictions including effects of the finite thickness of lens planes in the line-of-sight integration that mimic the setup of ray-tracing simulation (Takahashi et al. 2017) used in the mocks.

ξ_- since the full-sky lensing simulations have an effective angular resolution corresponding to $\ell \lesssim 4000$ (Takahashi et al. 2017). One can include this resolution effect in the model of lensing power spectrum (Eq. 5) as

$$P_{\kappa,ab}(\ell) \rightarrow P_{\kappa,ab}(\ell) \frac{1}{1 + (\ell/\ell_{\text{sim}})^2} \Theta(3N_{\text{SIDE}} - \ell), \quad (26)$$

where $\Theta(x)$ is the Heaviside step function, $\ell_{\text{sim}} = 1.6 \times N_{\text{SIDE}}$ and $N_{\text{SIDE}} = 8192$ (Takahashi et al. 2017). Apart from the angular resolution effect, we still find that the average ξ_{\pm} can be different from its expectation value of Eq. (8). The differences of ξ_+ at $\theta \gtrsim 1$ arcmin and ξ_- at $\theta \gtrsim 10$ arcmin in the bottom panels of Figure 3 can be explained by the finite thickness effect of projected density shells in ray-tracing simulations (Takahashi et al. 2017). We summarize the finite thickness effect on lensing power spectrum in Appendix B. Using Eqs. (26), (B3), and (B4), we obtain the theoretical model of ξ_{\pm} including the effective angular resolution and the finite thickness effect of projected density shells in the ray-tracing simulations. The dashed lines in Figure 3 show the corrected version of ξ_{\pm} and provide a better fit to the simulation results.

We now discuss the covariance of cosmic shear correlation functions that resemble the HSC S16A data. We first examine the theoretical model of the covariance matrix in Section 2.3 by comparing the prediction with the covariance estimated from 2268 mock realizations. To do this we use the mocks without galaxy shape noise, because we want to test whether the theoretical model can explain the mock covariance, from the linear to nonlinear scales. For the mocks without shape noise, we use the lensing shear for a given source galaxy in the mocks and set unit weight when computing the two-point correlation, but keeping the angular and redshift information fixed as in the real catalogue. Figure 4 shows the diagonal components of cosmic shear covariance in one of the HSC S16A

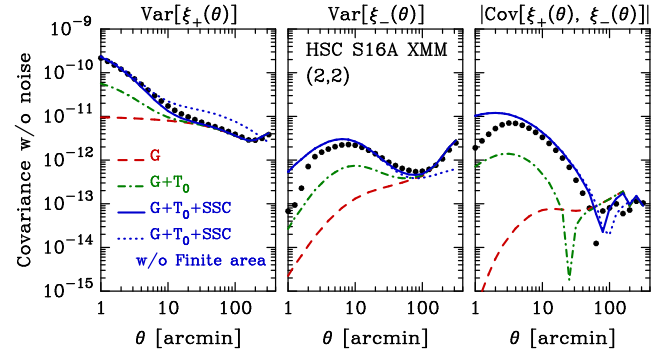


Figure 4. Comparison of the variance of cosmic shear correlation functions computed by the (semi-)analytical model and from the mock catalogues. As an example we consider the correlation function for source galaxies in the second tomographic redshift bins for one of the HSC fields, the XMM field. To study the impact of non-Gaussian sample variance, we ignore the shape noise contribution. The left, middle, and right panels show the variance of ξ_+ , the variance of ξ_- , and the cross variance between ξ_+ and ξ_- , respectively. In each panel, the black point shows the mock results. The colored lines show the different contributions in our analytical predictions; the red dashed lines show the Gaussian covariance, the blue solid lines are the non-Gaussian covariance, and the green dashed-dotted lines are the covariance without the SSC contribution. The dotted lines show the analytical predictions when ignoring effects of the survey boundary/footprint on the number of source galaxy pairs in the Gaussian variance calculation (see text for details and Appendix A). Note that the XMM field covers $\sim 34.1 \text{ deg}^2$.

fields, the XMM field, in the absence of shape noises. The black points in Figure 4 show the mock covariance from 2268 realizations, while different colored lines represent the theoretical prediction as in Section 2.3. To compute the theoretical prediction, we adopt a halo-model approach (Cooray & Hu 2001) as the relevant formulae are explicitly given in Appendix C. For a computation of the Gaussian covariance, we properly take into account the effect of finite survey area or survey geometry. To be more precise, we properly estimate the number of pairs of two source galaxies, separated by a given angle, that can be taken from the HSC survey footprint (the XMM field considered here), as shown in Eq. (A5). We then estimate the weighted average of ensemble-averaged correlation functions, ξ_{\pm} , to obtain the prediction for the Gaussian covariance. The blue solid lines are the analytical predictions which include all the contributions, i.e. the Gaussian and non-Gaussian covariance contributions. The figure shows that the analytical predictions fairly well reproduce the mock results over the range of scales we consider. On the other hand, the blue dashed lines show the model predictions when ignoring the finite area effect in the Gaussian covariance calculation or equivalently when using Eq. (12) (without shape noise), which is based on a naive estimation of the number of source galaxy pairs. Comparison of the solid and dashed blue lines manifests that an accurate prediction of the Gaussian covariance requires to include the effect of survey geometry in estimating the number of source galaxy pairs.

Next, we consider the case including the shape noise contribution to the covariance. To compute the shape noise contribution in the analytical model, we use Eqs. (12) and (13) to compute the terms including σ_{ϵ}^4 and $\sigma_{\epsilon}^2 P_{\kappa}$, where we ignore the effect of survey geometry. To do this, we use the effective number density of source galaxies in the HSC S16A XMM field following Eq. (1) in Heymans et al. (2012), where we take into account the lensing weights for HSC galaxies. For the sample variance of Gaussian covariance we use

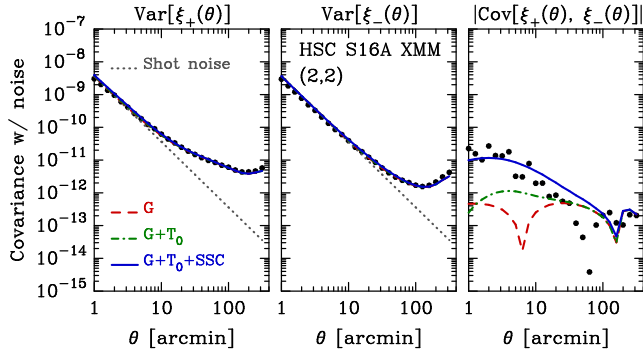


Figure 5. Similar to Figure 4, but the intrinsic shape is included here. The grey line represents the shot noise contribution alone.

the same method in Figure 4 (i.e. the method given in Appendix A). Figure 5 compares the analytical predictions with the mock results for the diagonal components in cosmic shear covariance. The simple analytical predictions fairly well reproduce the mock covariance which includes non-trivial observational effects such as the spatial and redshift distributions of source galaxies, the distribution of their distortions, and the lensing weights. Compared to Figure 4, the figure that the relative contribution of the non-Gaussian covariance to the shape noise covariance is weaker at $\theta < 10$ arcmin. Nevertheless, it should be noted that the non-Gaussian covariance, especially the SSC term, is important for the off-diagonal elements as well as the cross covariance between ξ_+ and ξ_- , even in the presence of the shape noise. We also note that the survey geometry effect on the sample variance of Gaussian covariance needs to be properly taken into account.

The upper or lower panel in Figure 6 shows the full covariance matrix of ξ_+ or ξ_- including all the 4 tomographic bins, respectively. In each panel, the upper-left triangle elements present the mock covariance, while the lower-right elements are the difference between the mock covariance and the analytical model prediction. For the Gaussian covariance computation in the analytical prediction, we used the same method as in Figure 5. The analytical model covariance is again in a qualitatively nice agreement with the mock results including the off-diagonal components, in spite of the several approximations. The accuracy of our model covariance is found to be the level of 20 – 30%. Thus Figures 4 – 6 demonstrate that we have a good understanding of the nature of cosmic shear covariance, and we will below use the mock catalogues for a further discussion of the cosmic shear covariance.

5.2 Field variations in clustering observables

Since each of our mock catalogues, generated from full-sky realizations, properly consists of 6 different fields in the HSC S16A data, we here quantify the impact of field variations on the cosmic shear covariance¹¹. To study this, we first measure the cosmic shear correlation function of source galaxies in a given combination of tomographic bins, denoted by a and b , from the field “ f ” of the r -th mock catalogue; we denote this correlation function as $\xi_{\pm,ab}^{(r)}(\theta; f)$.

¹¹ In this section, we focus on the field variation in the covariance. In Appendix D, we examine the field variation in the correlation functions themselves, ξ_{\pm} . We also note each field is separated from the others by 40 – 180 deg.

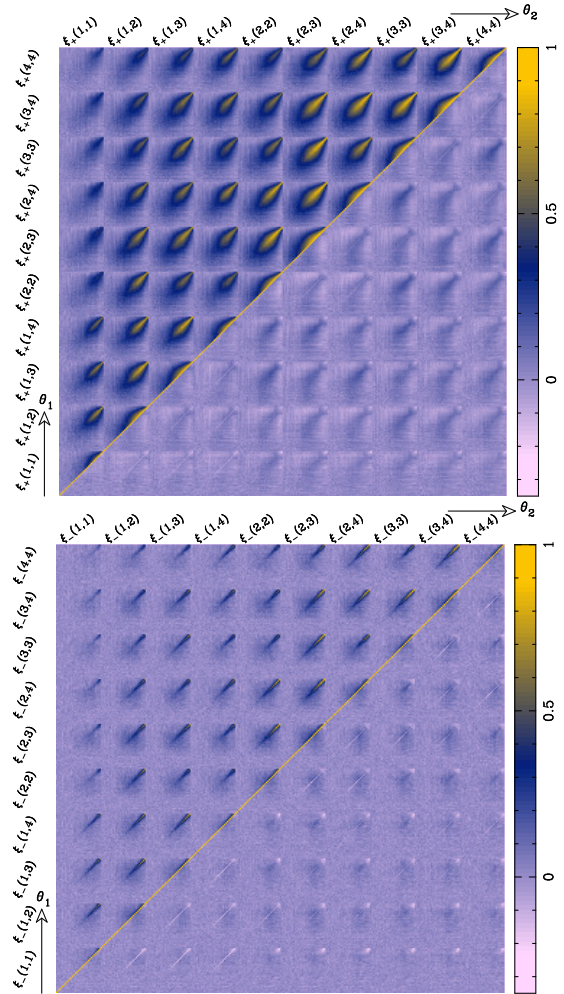


Figure 6. Comparison of the covariance matrices for ξ_{\pm} 's in four tomographic redshift bins (Fig. 1) computed by the analytical model and from the mock catalogues. The top panel shows the result of ξ_+ , while the bottom is for ξ_- . We here consider the HSC S16A XMM field alone, and include the shape noise contribution. In each panel, the upper-left triangular elements show the mock covariance, while the lower-right elements represent the difference between the mock result and our analytical prediction. Note the covariance matrix is normalized with the diagonal components. Our analytic covariance is consistent with the mock counterpart with a $\sim 20 - 30\%$ accuracy.

We then combine all the correlation functions in the 6 fields to estimate the “full” correlation function, denoted as $\xi_{\pm,ab}(\theta; \text{comb})$, for the entire HSC S16A fields:

$$\xi_{\pm,ab}^{(r)}(\theta; \text{comb}) = \frac{\sum_f N_p^{ab}(\theta; f) \xi_{\pm,ab}^{(r)}(\theta; f)}{\sum_f N_p^{ab}(\theta; f)}, \quad (27)$$

where $N_p^{ab}(\theta; f)$ is the effective number of source galaxy pairs used in the cosmic shear correlation estimation, defined in Eq. (10). Note that $N_p^{ab}(\theta; f)$ is the same in all the mock realizations since our mock catalogues use the same spatial distribution of source galaxies as in the real catalogue. The covariance matrix for the full correlation function can be estimated from all the mock realizations

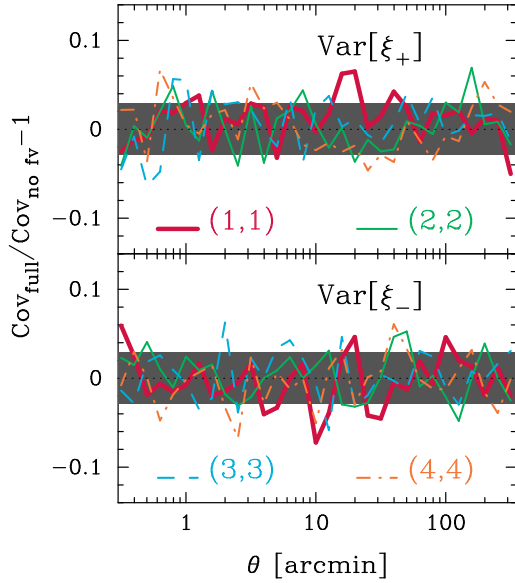


Figure 7. Impact of field variation on variance estimation of cosmic shear. The upper panel shows the effect of field variation in the variance of ξ_+ , while the lower represents the case for ξ_- . In each panel, we consider the fractional difference between the variance with and without the field variation. The variance including the field variation is defined in Eq. (28), while we estimate the variance in the absence of field variations with Eq. (30). Note that zero in y axis represents no impact of field variation. Different colored lines in each panel present the results with four different tomographic bins. The thick solid, thin solid, dashed, dashed-dotted lines represent the first, second, third, and fourth tomographic bin, respectively. Note that the grey filled region in each panel shows a statistical uncertainty in the variance estimation over 2268 realizations assuming a Gaussian distribution.

as

$$\text{Cov}_{\text{full}} [\xi_{\pm,ab}(\theta_i), \xi_{\pm,cd}(\theta_j)] = \frac{1}{N_{\text{rea}} - 1} \times \sum_{r=1}^{N_{\text{rea}}} \left\{ \xi_{\pm,ab}^{(r)}(\theta_i; \text{comb}) - \bar{\xi}_{\pm,ab}(\theta_i; \text{comb}) \right\} \times \left\{ \xi_{\pm,cd}^{(r)}(\theta_j; \text{comb}) - \bar{\xi}_{\pm,cd}(\theta_j; \text{comb}) \right\}, \quad (28)$$

where

$$\bar{\xi}_{\pm,ab}(\theta_i; \text{comb}) = \frac{1}{N_{\text{rea}}} \sum_{r=1}^{N_{\text{rea}}} \xi_{\pm,ab}^{(r)}(\theta_i; \text{comb}), \quad (29)$$

and $N_{\text{rea}} = 2268$ is the number of mock realizations.

For comparison, we also estimate the covariance matrix ignoring correlations between the cosmic shear correlation functions in the different fields as

$$\text{Cov}_{\text{no fv}} [\xi_{\pm,ab}(\theta_i), \xi_{\pm,cd}(\theta_j)] = \frac{\sum_{f=1}^{N_{\text{field}}} N_p^{ab}(\theta_i; f) N_p^{cd}(\theta_j; f) \text{Cov}_{\text{each}} [\xi_{\pm,ab}(\theta_i; f), \xi_{\pm,cd}(\theta_j; f)]}{\left(\sum_{f=1}^{N_{\text{field}}} N_p^{ab}(\theta_i; f) \right) \left(\sum_{f=1}^{N_{\text{field}}} N_p^{cd}(\theta_j; f) \right)}, \quad (30)$$

where Cov_{each} is the covariance of ξ_{\pm} in each of the 6 HSC fields that is estimated from our mock catalogues in the field.

Figure 7 shows the fractional difference between the two covariances of Eqs. (28) and (30). To be specific, we plot the quantity of $\text{Cov}_{\text{full}} / \text{Cov}_{\text{no fv}} - 1$. Here we present only the diagonal components for the auto correlations of the same tomographic bins, $\xi_{\pm,aa}$.

It can be found that the effect of field variations on the covariance is not significant for the HSC 16A data. To be more precise, the fractional difference is at a level of 3–5% over the range of angular scales. Note that a statistical uncertainty in the variance estimation assuming a Gaussian distribution is $\sqrt{2/N_{\text{rea}}} \sim 2.9\%$.

5.3 The impact of photo- z errors on cosmic shear covariance

Photo- z errors are one of the most severe systematic effects on cosmic shear cosmology. In this section, we study the impact of photo- z errors on the cosmic shear covariances using our mock catalogues. Besides our fiducial set up, we also generate the mock catalogues of galaxy shapes using the posterior photo- z distributions estimated using three different photo- z catalogues, ephor, frankenz, and mizuki. For this purpose we generate 210 realizations for each of the three catalogues.

To quantify the impact of photo- z errors on the cosmic shear covariance we use the differential signal-to-noise ratio of ξ_{\pm} at each angular bin θ , denoted as $(S/N)_{\text{bin}}^2$. For this purpose we generate the mock catalogues based on the following method in order to make an apple-to-apple comparison of the results from different photo- z catalogues. First, we use exactly the same number of source galaxies and the same realizations of full-sky simulations to simulate the lensing signals on each of source galaxies, for the four different photo- z catalogues (the fiducial plus the three catalogues). To be more precise, we inject each of source galaxies, taken from the HSC S16A XMM field, into a given realization of the full-sky simulations. In doing this, we randomly assign a redshift of each source galaxy from the photo- z posterior distribution for each of MLZ, ephor, frankenz, and mizuki, inject the galaxy into the nearest source plane of the simulation, and then simulate the lensing effect on the galaxy image (see Section 4.2). We repeat this procedure for all the source galaxies. We used 2,425,405 galaxies in total in each mock catalogue. The stacked posterior photo- z distributions for different methods are shown in the lower plot in Figure 8. The stacked redshift distributions display subtle different features from each other depending on which algorithm of photo- z code to use. Note that we do not consider a tomographic analysis in this subsection for simplicity.

The upper plot in Figure 8 shows the ratio of $(S/N)_{\text{bin}}^2$, obtained from each of the mock catalogues based on the different photo- z codes, relative to that of MLZ photo- z catalogue. The upper panel represents the results for ξ_+ , while the lower is for ξ_- . In each panel, the thick line shows the ratio of $(S/N)_{\text{bin}}^2$ when we include the changes of ξ_{\pm} and their variance by different $p(z)$, while the thin line corresponds to the case changing the variance alone and using the same signals as the MLZ case. It can be found that the different photo- z catalogues yield slightly different $(S/N)_{\text{bin}}^2$ by a ~ 5 -10% level.

From comparison of the thick and thin lines in the upper plot, it can be found that the change in the variance due to the different photo- z methods, keeping the signal fixed to the same, yields a 10-20% change in $(S/N)_{\text{bin}}^2$. If further including the change in the signal due to the different photo- z catalogues, the two effects are somewhat compensated, and the net change in $(S/N)_{\text{bin}}^2$ becomes smaller (within a 10% level over the range of scales). It would be worth noting that the shape noises in the sample used in Figure 8 are much smaller than one in tomographic analyses as in Figure 5. In Figure 8, the sample variance (including non-Gaussian terms) dominates the variance of ξ_{\pm} over the angular range of $\sim 3 - 100$ arcmin. Hence, when changing $p(z)$, the signal and their variance change in a similar way and the $(S/N)_{\text{bin}}^2$ is less affected effectively.

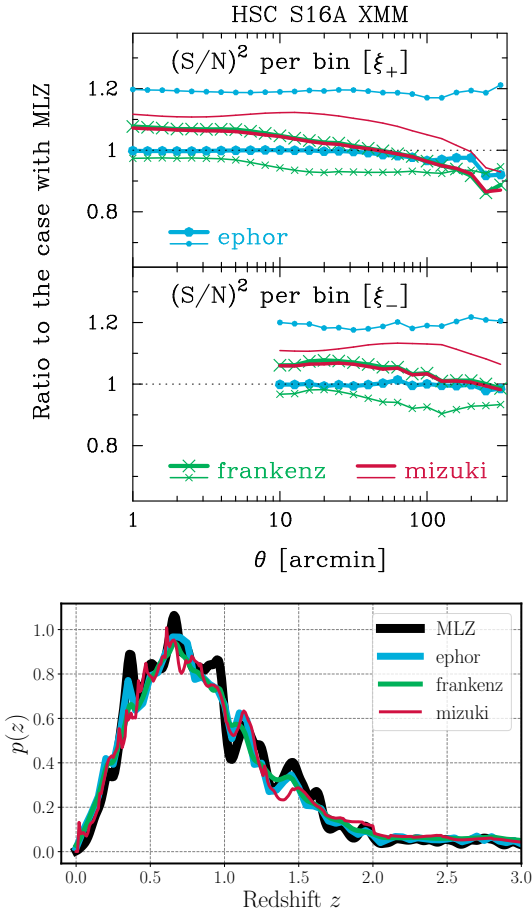


Figure 8. Impact of photo- z posterior distributions on variance estimation of cosmic shear. *Top:* The upper panel shows the signal-to-noise ratio (S/N) of ξ_+ for a given θ , while the lower represents the case for ξ_- . In each panel, we consider the ratio of $(S/N)^2$ with three different photo- z posterior distributions $p(z)$ to the counterpart with MLZ. Cyan lines with circle, green lines with cross symbol, and red solid lines represent the results with $p(z)$ from ephor, frankenz, and mizuki, respectively. Hence, one in y axis means there are no differences in S/N when one changes the $p(z)$ from MLZ to other. Since we can not have a reasonable estimate of mean ξ_- at $\theta \lesssim 10$ arcmin, we restrict the results for $\theta > 10$ arcmin in the lower panel. For comparison, the thin lines in upper and lower panels show the results when we change the variance according to photo- z methods but keep the signal fixed to the MLZ case. *Bottom:* The photo- z posterior distributions from different methods used in the top panels.

Assuming less source number density as in Figure 5, we expect that the $(S/N)_{\text{bin}}^2$ at $\theta \lesssim 10$ arcmin can change with a level of 10 – 20% according to different $p(z)$ since the shape noise dominates the variance at those angular scales. Nevertheless, the $(S/N)_{\text{bin}}^2$ at the sample-variance dominated regime will be still less affected as shown in Figure 8 as long as one use an appropriate $p(z)$ for both of signals and their covariance.

5.4 Signal-to-noise ratio

A large set of the HSC mock catalogues enables us to estimate an expected, cumulative signal-to-noise ratio for a measurement of the cosmic shear correlation functions from the HSC S16A data. Assuming four tomographic redshifts bins (see Figure 1), we construct a data vector of \mathbf{D} from different combinations of

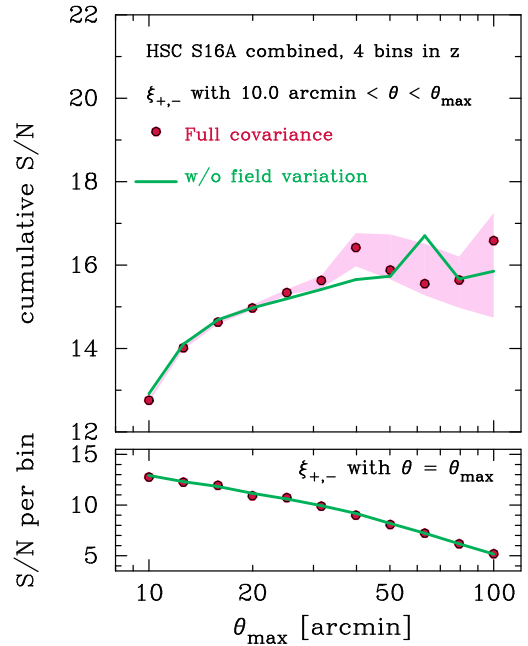


Figure 9. The expected signal-to-noise ratio of tomographic cosmic shear analysis with 4 bins in HSC S16A. The upper panel shows the cumulative signal-to-noise ratio (S/N) as a function of maximum angular scales θ_{max} . In the upper panel, we set the minimum scale to be 10 arcmin and use 10 tomographic ξ_+ and ξ_- . Pink filled region in the upper panel show the results from 108 bootstrap samplings of 2247 measurements of ξ_{\pm} . The lower panel represent the S/N for a given angular scale, but we put together with 10 possible tomographic bins. In each panel, the red points show the S/N with full covariance from 2268 mock realizations, while the green lines present the S/N in the absence of field variations.

the cosmic shear correlation functions given as a function of angular bins and tomographic bins, $\xi_{\pm,ab}(\theta_i)$ over the angular range of $10 \leq \theta_i$ [arcmin] ≤ 100 . We adopt up to 11 angular bins in the angular range and have 10 correlation functions for each of ξ_{\pm} at each angular bin that are available from combinations of the 4 redshift bins; therefore, the dimension of data vector $220 = 10 \times 11 \times 2$ at maximum. The cumulative signal-to-noise ratio up to a maximum angular scale θ_{max} is defined as

$$\left(\frac{S}{N}\right)_{\text{cum}}^2 [\theta_{\text{max}}] = \sum_{\theta_{\text{min}} \leq \{\theta_i, \theta_j\} \leq \theta_{\text{max}}} \sum_{p,q} {}^t \bar{\mathbf{D}}(\theta_i; p) \mathbf{C}^{-1} \bar{\mathbf{D}}(\theta_j; q), \quad (31)$$

where $\theta_{\text{min}} = 10$ arcmin, \mathbf{C} is the covariance matrix of data vector \mathbf{D} , $\bar{\mathbf{D}}$ is the expectation value of \mathbf{D} , ${}^t \bar{\mathbf{D}}$ is the transposed vector of $\bar{\mathbf{D}}$, and p and q represent the indexes of tomographic bins in ξ_{\pm} . For the data vector $\bar{\mathbf{D}}$, we use the averaged ξ_{\pm} over 2268 mock realizations. We also study the differential signal-to-noise ratio at a given angular bin, θ , defined as

$$\left(\frac{S}{N}\right)_{\text{bin}}^2 = \sum_{p,q} {}^t \bar{\mathbf{D}}(\theta; p) \mathbf{C}^{-1} \bar{\mathbf{D}}(\theta; q). \quad (32)$$

Note that, when estimating the inverse matrix \mathbf{C}^{-1} in Eqs. (31) and (32), we included the correction factor of $N_{\text{rea}}/[N_{\text{rea}} - N_D - 1]$ proposed in Hartlap et al. (2007), where N_{rea} is the number of the realizations and N_D is the dimension of data.

Figure 9 shows the results for the cumulative or differential S/N value expected for the HSC S16A data. In this figure, we

use two different covariance matrices; one is the full covariance evaluated with Eq. (28), and another is the covariance in the absence of field variation among six different HSC S16A fields, defined as Eq. (30). The figure shows the cumulative signal-to-noise ratio in HSC S16A cosmic shear analyses is expected to be 16 – 17 if the cosmology assumed in our simulations is correct. The field variation is found to be less important for estimation of signal-to-noise ratio at a given angular scale, but it can induce a 6 – 7% difference in the total signal-to-noise ratio if the correlation functions ξ_{\pm} at scales around 1 degree are included. To study the scatter in the signal-to-noise ratio, we perform bootstrap sampling of 2247 mock catalogues 108 times¹² and then measure the cumulative signal-to-noise ratio for each bootstrap realization. The pink filled region represents the bootstrap results and indicate the scatter in the evaluation of the cumulative signal-to-noise ratio in our mocks. The difference between the red point and the green line in the upper panel of Figure 9 is still comparable to the bootstrap scatter, indicating that the difference can be consistent with a statistical fluke. We further comment on the result of cumulative S/N in Figure 9. We find the field variation can change the off-diagonal components in the covariance of ξ_+ and the cross covariance between ξ_+ and ξ_- . Including the field variance is found to increase the cumulative S/N of ξ_+ in our tomographic analysis with a level of 2 – 3% compared to the case in the absence of field variation, but it does not affect ξ_- . We also confirm that the cumulative S/N of ξ_+ or ξ_- monotonically increases as a function of θ_{\max} , while the cross covariance between ξ_+ and ξ_- would induce the complex feature in the cumulative S/N of four-tomographic ξ_{\pm} at $\theta_{\max} > 40 - 50$ arcmin. In addition, the bootstrap scatter in the cumulative S/N of ξ_{\pm} at $\theta_{\max} > 50$ arcmin is of an order of 5 – 10%, while the Gaussian uncertainty of covariance with 2247 realizations is $\sim 2.9\%$. This implies that the degree-scale ξ_{\pm} in tomographic analysis of the HSC S16A data will be non-Gaussian and may break a common approximation in cosmological likelihood analyses (also see the following subsection).

5.5 Likelihood function for parameter inference

The cosmological parameter estimation with cosmic shear requires a likelihood function of correlation functions ξ_{\pm} . Although the likelihood function is assumed to be Gaussian in practice, recent studies claim that the likelihood function of cosmic shear correlation functions can be skewed (e.g. Sellentin et al. 2018) and Gaussian assumption may affect the cosmological parameter estimation with cosmic shear (e.g. Hartlap et al. 2009; Sato et al. 2010). Hence, it is worth studying if the non-Gaussian likelihood function can matter in the cosmic shear analyses with HSC S16A. To quantify the non-Gaussianity in cosmic-shear likelihood and evaluate its impact on parameter estimation, we define so-called chi squared quantity χ^2 as

$$\chi^2 \equiv \sum^t (\mathbf{D} - \bar{\mathbf{D}}) \mathbf{C}^{-1} (\mathbf{D} - \bar{\mathbf{D}}), \quad (33)$$

where the summation runs over all the angular bins in the range of $10 \leq \theta[\text{arcmin}] \leq 100$ and possible tomographic bins over four different source redshift bins. Note that the quantity of χ^2 can be set for individual realizations of mock catalogue and it should follow the χ^2 distribution with 220 degrees of freedom if \mathbf{D} follows Gaussian.

¹² Note that we extract 21 HSC S16A fields from a single full sky and the number of full-sky simulations is 108. Hence, it is easiest to construct 108 bootstrap samples of $107 \times 21 = 2247$ mocks in our configuration.

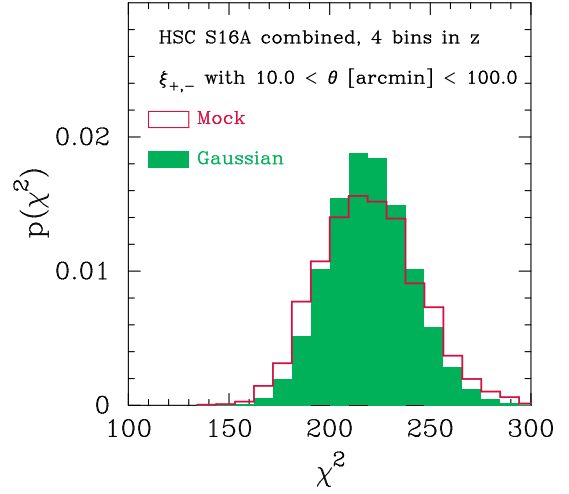


Figure 10. Probability distribution function (pdf) of chi squared value in HSC cosmic shear tomography. The definition of chi squared is found in the text. We here assume four different tomographic bins and combine 6 patches in HSC S16A. Red open histogram shows the pdf obtained from 2268 mock realizations, while green filled histogram represents the expectation from Gaussian cosmic shear correlations. In this figure, we use the correlation functions ξ_{\pm} in the range of $10 \leq \theta[\text{arcmin}] \leq 100$. We have two correlations of ξ_{\pm} with 11 bins in θ and 10 bins in redshifts, leading the degrees of freedom to be $2 \times 11 \times 10 = 220$.

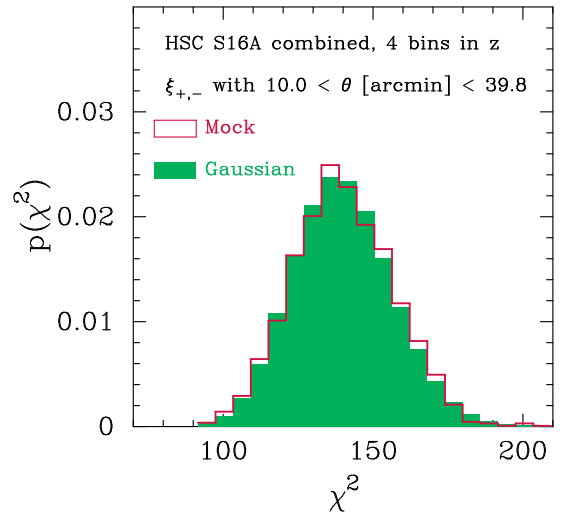


Figure 11. Similar to Figure 10, but we restrict the angular range of 10 – 40 arcmin. Here we have two correlations of ξ_{\pm} with 7 bins in θ and 10 bins in redshifts, leading the degrees of freedom to be $2 \times 7 \times 10 = 140$.

Figure 10 shows the histogram of χ^2 that is computed from 2268 mock catalogues for a hypothetical measurement of the HSC S16A cosmic shear correlation functions. In this figure, green filled histogram represents the Gaussian prediction, while red line shows the mock results. This figure shows the non-Gaussian likelihood of cosmic shear correlations could broaden a confidence level in a parameter estimation (e.g. an amplitude parameter such as S_8). We find that the mean value of χ^2 over 2268 realizations is 219.03 and it is in good agreement with simple Gaussian expectation, while the variance of χ^2 in our mock catalogues is found to be 627.86, corresponding to 1.42 times as large as Gaussian prediction. For a 95% confidence level, the interval in mock χ^2 should range from

181.173 to 230.495, while their Gaussian counterparts are 209.686 and 228.273, respectively.

The red open histogram in Figure 10 is also found to be explained by a modified χ^2 distribution as

$$p(\chi^2, N_{\text{dof}}) = f(\chi^2 - N_{\text{dof}} + k, k), \quad (34)$$

where $f(x, k)$ is the χ^2 distribution with k degrees of freedom. When setting to $N_{\text{dof}} = 220$, we find $k = 315$ can explain the broadening of the histogram of χ^2 in Figure 10. According to the above, we will discuss the effective number of degrees of freedom in the HSC S16A cosmic shear analyses. Since the signal-to-noise ratio of χ^2 with k degrees of freedom is given by $k/\sqrt{2k}$, the effective degrees of freedom $k_{\text{eff}} \sim 220^2/315 = 153.6$ gives the similar signal-to-noise ratio of χ^2 in our mock analyses. This computation of effective degrees of freedom implies that the effective number of angular bins per tomographic bin will be $153.6/10 \sim 7.68$. Since we have 11 bins in θ in Figure 10, the largest 3–4 bins in θ may be effectively less important for the evaluation of χ^2 . A principal component analysis will be required to study how the different ξ_{\pm} are correlated with each other and how many independent bins contribute to most of the information contents in more details (e.g. Kayo et al. 2013). Note that we do not include the correction factor to invert \mathbf{C} as in Hartlap et al. (2007) in Figure 10. When we include the correction, the red open histogram shifts to right with a level of 10%, but the 95% confidence level is still wider than its Gaussian counterpart. It is also worth noting that Eq. (34) is not a unique expression to characterize the non-Gaussianity in likelihood function of cosmic shear two-point correlations. Appropriate treatment of non-Gaussian likelihood may be needed to extract all information of cosmic shear two-point correlations, while it is beyond the scope of this paper.

On the other hand, Figure 11 shows the histogram of χ^2 in 2268 realizations of mock cosmic shear analyses when we use the information at the angular range of 10–40 arcmin. Comparing with Figures 10 and 11, we conclude the degree-scale ξ_{\pm} can broaden the width of the histogram in χ^2 in our mock catalogues. Once we focus on the angular range of $\theta = 10 - 40$ arcmin, the histogram of χ^2 in our mocks follows the expected χ^2 distribution (Similar results are found in Sellentin et al. 2018). Figures 10 and 11 demonstrate that our mock catalogues allow to set the angular scales at which a Gaussian likelihood approximation is valid.

5.6 Impact of non-zero multiplicative bias

So far, we assumed the multiplicative bias in the shear of each object in mock catalogues to be zero. In this subsection, we examine the impact of non-zero multiplicative bias in the tomographic correlation analysis of cosmic shear in the HSC S16A. Note that we still assume zero additive biases in this subsection.

Since the correction of multiplicative bias is valid for the average shape over a given sample of source galaxies, we need to be careful when including the multiplicative bias on object-by-object basis. In this paper, we propose the following modification in lensing shear when incorporating with simulation and observed data sets as in Eqs. (24) and (25):

$$\gamma \rightarrow (1 + \langle m \rangle) \gamma, \quad (35)$$

where γ represents the lensing shear from full-sky ray-tracing simulation and $\langle m \rangle$ is the average multiplicative bias for the galaxy sample of interest. When working on four tomographic bins, we will have four different values of $\langle m \rangle$. For galaxies at i -th tomographic bin, we use the corresponding multiplicative bias $\langle m_i \rangle$ to

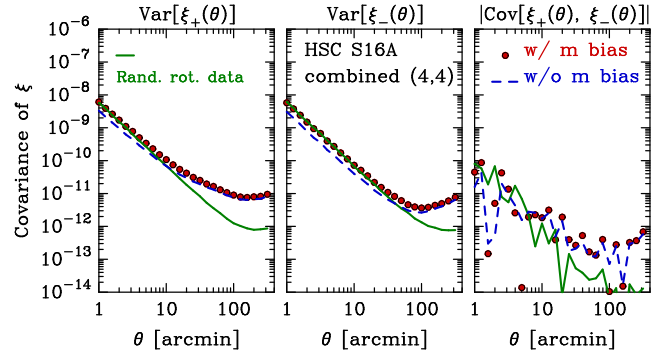


Figure 12. Impact of multiplicative bias on the covariance of cosmic shear correlation functions. As a representative example, we consider the correlation function for source galaxies in the fourth tomographic redshift bin. In each panel, the red points show the diagonal covariance estimated from the mock catalogues with non-zero multiplicative bias, while the blue dashed line represent the mock covariance when the multiplicative bias is set to be zero in mock catalogues. As a reference, the green solid line in each panel shows the covariance by the actual data but each shape in the catalogue is randomly rotated. Hence, the green solid line should represent the shape noise term in covariance alone. Including multiplicative bias can boost the amplitude of shape noise in cosmic shear analysis, but the large-scale covariance is less affected by the presence of non-zero multiplicative bias.

produce the mock distortion. This simple procedure enables us to keep the shear responsivity fixed regardless of the value of multiplicative bias.

At the lowest-order level of Eqs. (24) and (25), the mock distortion can be expressed as

$$\epsilon^{\text{mock}} \simeq \epsilon^{\text{int}} + \epsilon^{\text{mea}} + 2\mathcal{R}(1 + \langle m \rangle)\gamma. \quad (36)$$

To obtain an unbiased estimate of lensing shear from ϵ^{mock} , we will use $\epsilon^{\text{mock}}/(2\mathcal{R})/(1 + \langle m \rangle)$, but this correction leads the effective shape noise $(\epsilon^{\text{int}} + \epsilon^{\text{mea}})/(2\mathcal{R})$ changes by a factor of $(1 + \langle m \rangle)^{-1}$. Therefore, including non-zero multiplicative biases remains the estimator of ξ_{\pm} unbiased as long as one include the correction of $(1 + \langle m \rangle)^{-1}$ to the observed distortion, while the covariance of ξ_{\pm} should be affected by non-zero $\langle m \rangle$.

Figure 12 highlights the impact of non-zero multiplicative bias on the covariance of ξ_{\pm} in the HSC S16A. In this figure, we show the variance of ξ_{\pm} and the cross variance between two when including non-zero multiplicative biases for the fourth tomographic redshift bin of source galaxy sample in the HSC S16A. The red points in the figure show the results in the presence of non-zero $\langle m \rangle$, while the blue dashed line corresponds to the cases with $\langle m \rangle = 0$. Note that we find $\langle m \rangle$ has a negative value over six HSC S16A fields and four tomographic bins. Hence, the effective shape noise should increase in our four-tomographic analysis when we include the non-zero $\langle m \rangle$. As a reference, the green dashed lines in this figure show the covariance estimated from randomly rotated shapes in real HSC S16A data. Comparing with the red points and the green solid lines, we confirm that the small-scale covariance can increase due to the change of the effective shape noise. On the other hand, the large-scale covariance is less affected by the presence of non-zero $\langle m \rangle$, since the sample variance should dominate at degree scales and it is independent of the amplitude of shape noise.

Figure 13 demonstrates the impact of non-zero multiplicative bias of signal-to-noise ratio of cosmic shear analysis in the HSC S16A, which is an indicator of cosmological information contents in the analysis. When combining all HSC S16A fields and four

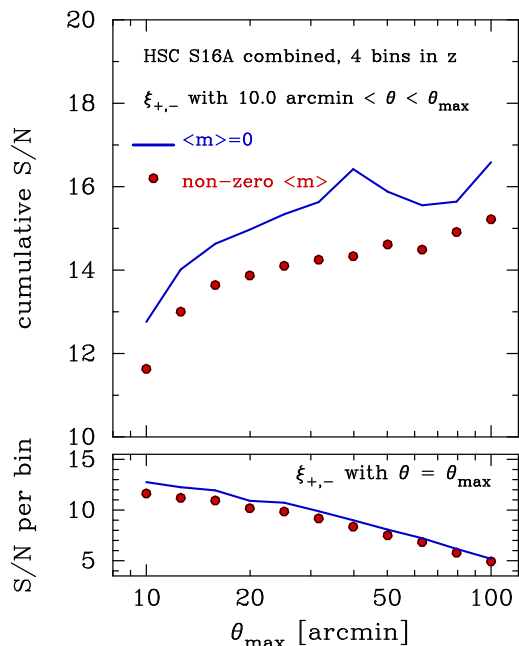


Figure 13. Similar to Figure 9, but we include the non-zero multiplicative biases in our HSC mock catalogues. In each panel, the red points show the results in the presence of non-zero multiplicative biases and the blue solid lines are for zero multiplicative biases. For the tomographic cosmic shear analysis in HSC S16A, including the non-zero multiplicative bias can degrade the cumulative signal-to-noise ratio with $\approx 20\%$ level.

tomographic bins in the angular range of 10 – 100 arcmin, we find the non-zero multiplicative bias can affect the cumulative signal-to-noise ratio by $\sim 20\%$ in the HSC S16A. It would be worth noting that the impact of multiplicative bias on the shape noise depends on the sign of multiplicative bias. If the multiplicative bias can have a positive value, the effective shape noise will be reduced by a factor of $(1 + \langle m \rangle)^{-1} \approx (1 - \langle m \rangle)$. Since the value of $\langle m \rangle$ depends on galaxy selection for a given shape catalogue, we need to prepare the mock catalogues with an appropriate $\langle m \rangle$ on analysis-by-analysis basis in practice.

6 CONCLUSIONS

In this paper, we have presented a set of mock catalogues of galaxy shapes in the first-year Subaru Hyper Suprime-Cam (HSC) data, referred to as HSC S16A. We produced the mock catalogues constructed from full-sky gravitational lensing simulations in Takahashi et al. (2017) and properly incorporated them with the observed galaxy information, allowing us to include various non-trivial effects in our mock catalogues. By construction, our mock catalogues can include inhomogeneous angular distribution of source galaxies, statistical uncertainty in photometric redshift (photo- z) estimate of each galaxy, variations in the lensing weights due to observational conditions, and the noise in galaxy shape measurement induced by both of intrinsic shape and measurement uncertainty. Using 2268 realizations of our mock catalogues in the footprint of HSC S16A, we performed a realistic analysis of galaxy-shape auto correlation functions ξ_{\pm} with tomographic redshift information and predicted one of the most important statistical properties in the current cosmological parameter inference, the covariance matrices of ξ_{\pm} . We compared the statistical property of ξ_{\pm} in our mock catalogues with

a theoretical model including the effect of nonlinear evolution in the matter density perturbations over cosmic time. Furthermore, we studied several effects on the cosmological analyses of cosmic shear correlation functions, including field variations among separated observed footprints, photo- z uncertainty of individual source galaxies, and non-Gaussianity in the likelihood function. Our findings are summarized as follows:

(i) The ensemble average of shape correlation functions ξ_{\pm} in our mock catalogues are consistent with a theoretical prediction based on the fitting formula of non-linear matter power spectrum (Takahashi et al. 2012) within a $< 10\%$ level accuracy. The discrepancy from theoretical predictions can be explained by the finite angular resolution and sampling effect in comoving distance in the ray-tracing simulations in Takahashi et al. (2017). Once the simulation-related effects are properly included, the ensemble average of ξ_{\pm} over our mocks is in agreement with its expectation with a level of 2 – 3%.

(ii) A theoretical model based on halo-model approach (e.g. Cooray & Hu 2001; Takada & Jain 2009; Takada & Hu 2013) is in good agreement with the mock covariance of ξ_{\pm} at angular separations less than 10 arcmin, whereas some corrections are required for the Gaussian covariance prediction in Joachimi et al. (2008). The corrections arise from finite sampling of source galaxies in a limited sky coverage. Once the corrections are included, the Gaussian covariance can provide a good fit to the mock covariance at degree scales. We also found the non-Gaussian covariance coming from the mode coupling between super-survey and sub-survey modes are dominant in the mock covariance at $\theta < 10$ arcmin, while another term from the four-point correlations within a given survey window is less important (also, see Barreira et al. 2018).

(iii) We studied the effect of field variance among six separated patches in HSC S16A on the covariance of ξ_{\pm} . Based on 2268 realizations, we found a 3 – 5% level difference in the mock variance when we removed the effect of field variations on an estimator of covariance (see Figure 7). Since the Gaussian uncertainty in the variance is estimated to be $\sqrt{2/2268} \sim 2.9\%$, we concluded that the field variation in the current HSC survey is less important for the covariance estimation.

(iv) In addition to our fiducial photo- z estimate, we also considered three different photo- z estimates obtained from different photo- z pipelines and applied them to the mock catalogue production. We then compared the signal-to-noise ratio of ξ_{\pm} at a given angular separation over four different photo- z estimates for a fixed source selection. We found a $\sim 5\%$ difference in the signal-to-noise ratio depending on the method of photo- z estimation (see Figure 8). Our results show the systematic uncertainty due to photo- z estimation will be a minor issue in the covariance estimation of ξ_{\pm} in HSC S16A data, if one adopt the photo- z estimates for the estimation of expectation value and their covariance in a self-consistent way.

(v) We predicted the total (cumulative) signal-to-noise ratio of cosmic shear correlation functions in an angular range of $\theta = 10 - 100$ arcmin with four tomographic bins based on our mock catalogues. We found the expected signal-to-noise ratio to be $\sim 16 - 17$ if our fiducial cosmological model would be correct and there are no multiplicative biases. A $\sim 6\%$ difference has been found in our mock catalogues when we ignore the field variance among six separated patches in HSC S16A, while the difference is still comparable to the scatter in the evaluation of signal-to-noise ratio based on bootstrap sampling.

(vi) Cosmological parameter inference with cosmic shear correlation relies on the chi-squared quantity defined as Eq. (33). When data of interest follows Gaussian, the chi-squared quantity should follow the chi-squared distribution with degrees of freedom being the number of data bins. We validated if the chi-squared quantity for ξ_{\pm} in HSC S16A can follow the expected distribution. We found the variance of the chi-squared quantity evaluated from 2268 mock realizations are 1.42 times as large as the simple expectation based on the number of data bins. In addition, the lower limit of 95% confidence interval in the chi-squared quantity in our mock moves downward by $\sim 10\%$ compared to the expectation from the relevant chi-squared distribution (see Figure 10). We also found the degree-scale correlation functions induce the deviation from Gaussianity in likelihood function.

(vii) We proposed a simple method to include non-zero multiplicative biases $\langle m \rangle$ in mock shape catalogues while keeping the shear responsivity fixed. Applying this method to tomographic cosmic shear correlation analysis in the HSC S16A, we examined the impact of multiplicative biases on the covariance. We found that the effective shape noise term can change by a factor of $(1 + \langle m \rangle)^{-1}$. Hence, the small-scale covariance of cosmic shear correlation functions can be affected by the presence of non-zero $\langle m \rangle$. For the HSC S16A cosmic shear correlation analysis with four tomographic redshift bins, we found the cumulative signal-to-noise ratio can degrade by $\simeq 20\%$ level when including non-zero $\langle m \rangle$ to estimate the covariance.

Since our mock catalogues take into account a lot of relevant features in galaxy shape measurement, one can utilize them for various purposes. Those include the covariance estimation of *any* cosmic shear statistics (e.g. Kilbinger 2015, for a recent review), and validation of analysis pipeline for parameter estimation (e.g. see Krause et al. 2017, for the representative work). In spite of our effort making the mock catalogues realistic as possible, there still remain some room for developing more realistic mock catalogues of galaxy shapes. An important feature missed in our mock catalogues is the correlation between property of source galaxy and matter density distribution at the redshift which the source galaxy locates. Intrinsic alignment (IA) effect of galaxy shape is among the most typical effects (Hirata & Seljak 2004; Troxel & Ishak 2015) and future work should include the IA effect properly. Also, source-lens clustering effects (Hamana et al. 2002) and magnification effects on observed galaxy (Schmidt et al. 2009; Liu et al. 2014) can be an issue in mock catalogue production for future lensing surveys.

Mock catalogue for modern galaxy survey should be also available for covariance estimation of cross correlation analyses of galaxy shapes with large-scale structures. For this purpose, one needs to construct a synthetic catalogue of tracers of large-scale structures and preserve the statistical correlation between galaxy shapes in mock catalogue productions. Since our mock shape catalogues are based on full-sky lensing simulations and their inherent halo catalogues are also available, we can construct mock catalogues of foreground objects for cross correlation with HSC S16A galaxy shapes by using a similar technique as in Shirasaki et al. (2017b). We leave it for our future work to create the mock catalogues of tracers of large-scale structures, that are correlated with mock shape catalogues in this paper.

ACKNOWLEDGMENTS

This work is in part supported by MEXT Grant-in-Aid for Scientific Research on Innovative Areas (No. 15H05887, 15H05893, 15K21733), by MEXT KAKENHI Grant Number (15H03654, 18H04358), and by JSPS Program for Advancing Strategic International Networks to Accelerate the Circulation of Talented Researchers.

The Hyper Suprime-Cam (HSC) collaboration includes the astronomical communities of Japan and Taiwan, and Princeton University. The HSC instrumentation and software were developed by the National Astronomical Observatory of Japan (NAOJ), the Kavli Institute for the Physics and Mathematics of the Universe (Kavli IPMU), the University of Tokyo, the High Energy Accelerator Research Organization (KEK), the Academia Sinica Institute for Astronomy and Astrophysics in Taiwan (ASIAA), and Princeton University. Funding was contributed by the FIRST program from Japanese Cabinet Office, the Ministry of Education, Culture, Sports, Science and Technology (MEXT), the Japan Society for the Promotion of Science (JSPS), Japan Science and Technology Agency (JST), the Toray Science Foundation, NAOJ, Kavli IPMU, KEK, ASIAA, and Princeton University.

The Pan-STARRS1 Surveys (PS1) have been made possible through contributions of the Institute for Astronomy, the University of Hawaii, the Pan-STARRS Project Office, the Max-Planck Society and its participating institutes, the Max Planck Institute for Astronomy, Heidelberg and the Max Planck Institute for Extraterrestrial Physics, Garching, The Johns Hopkins University, Durham University, the University of Edinburgh, Queen's University Belfast, the Harvard-Smithsonian Center for Astrophysics, the Las Cumbres Observatory Global Telescope Network Incorporated, the National Central University of Taiwan, the Space Telescope Science Institute, the National Aeronautics and Space Administration under Grant No. NNX08AR22G issued through the Planetary Science Division of the NASA Science Mission Directorate, the National Science Foundation under Grant No. AST-1238877, the University of Maryland, and Eotvos Lorand University (ELTE).

This paper makes use of software developed for the Large Synoptic Survey Telescope. We thank the LSST Project for making their code available as free software at <http://dm.lsst.org>.

Based [in part] on data collected at the Subaru Telescope and retrieved from the HSC data archive system, which is operated by the Subaru Telescope and Astronomy Data Center at National Astronomical Observatory of Japan.

Numerical computations were in part carried out on Cray XC30 and XC50 at Center for Computational Astrophysics, National Astronomical Observatory of Japan, and on XC40 at YITP in Kyoto University.

REFERENCES

- Aihara H., et al., 2018, *PASJ*, **70**, S4
- Barreira A., Krause E., Schmidt F., 2018, preprint, ([arXiv:1807.04266](https://arxiv.org/abs/1807.04266))
- Bartelmann M., Schneider P., 2001, *Physics Reports*, **340**, 291
- Becker M. R., 2013, *MNRAS*, **435**, 115
- Becker M. R., et al., 2016, *Phys. Rev. D*, **94**, 022002
- Bernstein G. M., Jarvis M., 2002, *AJ*, **123**, 583
- Cooray A., Hu W., 2001, *ApJ*, **554**, 56
- Coupon J., Czakon N., Bosch J., Komiyama Y., Medezinski E., Miyazaki S., Oguri M., 2018, *PASJ*, **70**, S7
- Diemer B., Kravtsov A. V., 2015, *ApJ*, **799**, 108
- Eifler T., Krause E., Schneider P., Honscheid K., 2014, *MNRAS*, **440**, 1379

Fosalba P., Gaztañaga E., Castander F. J., Manera M., 2008, *MNRAS*, **391**, 435

Friedrich O., Eifler T., 2018, *MNRAS*, **473**, 4150

Friedrich O., Seitz S., Eifler T. F., Gruen D., 2016, *MNRAS*, **456**, 2662

Furusawa H., et al., 2018, *PASJ*, **70**, S3

Górski K. M., Hivon E., Banday A. J., Wandelt B. D., Hansen F. K., Reinecke M., Bartelmann M., 2005, *ApJ*, **622**, 759

Hamana T., Mellier Y., 2001, *MNRAS*, **327**, 169

Hamana T., Colombi S. T., Thion A., Devriendt J. E. G. T., Mellier Y., Bernardeau F., 2002, *MNRAS*, **330**, 365

Harnois-Déraps J., van Waerbeke L., 2015, *MNRAS*, **450**, 2857

Harnois-Déraps J., Vafaei S., Van Waerbeke L., 2012, *MNRAS*, **426**, 1262

Harnois-Déraps J., et al., 2018, *MNRAS*, **481**, 1337

Hartlap J., Simon P., Schneider P., 2007, *A&A*, **464**, 399

Hartlap J., Schrabback T., Simon P., Schneider P., 2009, *A&A*, **504**, 689

Heymans C., et al., 2012, *MNRAS*, **427**, 146

Hikage C., et al., 2018, preprint, p. arXiv:1809.09148 (arXiv:1809.09148)

Hildebrandt H., et al., 2017, *MNRAS*, **465**, 1454

Hinshaw G., et al., 2013, *ApJS*, **208**, 19

Hirata C., Seljak U., 2003, *MNRAS*, **343**, 459

Hirata C. M., Seljak U., 2004, *Physical Review D*, **70**, 063526

Ichiki K., Takada M., Takahashi T., 2009, *Phys. Rev. D*, **79**, 023520

Joachimi B., Schneider P., Eifler T., 2008, *A&A*, **477**, 43

Kamada A., Shirasaki M., Yoshida N., 2014, *Journal of High Energy Physics*, **6**, 162

Kayo I., Takada M., Jain B., 2013, *MNRAS*, **429**, 344

Kilbinger M., 2015, *Reports on Progress in Physics*, **78**, 086901

Kilbinger M., Bonnett C., Coupon J., 2014, athena: Tree code for second-order correlation functions, Astrophysics Source Code Library (ascl:1402.026)

Köhlinger F., et al., 2017, *MNRAS*, **471**, 4412

Komiyama Y., et al., 2018, *PASJ*, **70**, S2

Krause E., Eifler T., 2017, *MNRAS*, **470**, 2100

Krause E., et al., 2017, preprint, (arXiv:1706.09359)

Li Y., Hu W., Takada M., 2014, *Phys. Rev. D*, **90**, 103530

Limber D. N., 1954, *ApJ*, **119**, 655

Liu J., Haiman Z., Hui L., Kratochvil J. M., May M., 2014, *Phys. Rev. D*, **89**, 023515

Mandelbaum R., 2017, preprint, (arXiv:1710.03235)

Mandelbaum R., et al., 2005, *MNRAS*, **361**, 1287

Mandelbaum R., Slosar A., Baldauf T., Seljak U., Hirata C. M., Nakajima R., Reyes R., Smith R. E., 2013, *MNRAS*, **432**, 1544

Mandelbaum R., et al., 2018a, *PASJ*, **70**, S25

Mandelbaum R., et al., 2018b, *MNRAS*, **481**, 3170

Markovic K., Bridle S., Slosar A., Weller J., 2011, *J. Cosmology Astropart. Phys.*, **1**, 022

Massey R., et al., 2013, *MNRAS*, **429**, 661

Miralda-Escude J., 1991, *ApJ*, **380**, 1

Miyazaki S., et al., 2015, *ApJ*, **807**, 22

Miyazaki S., et al., 2018, *PASJ*, **70**, S1

Navarro J. F., Frenk C. S., White S. D. M., 1996, *ApJ*, **462**, 563

Oguri M., et al., 2018, *PASJ*, **70**, S26

Sato M., Hamana T., Takahashi R., Takada M., Yoshida N., Matsubara T., Sugiyama N., 2009, *ApJ*, **701**, 945

Sato M., Ichiki K., Takeuchi T. T., 2010, *Physical Review Letters*, **105**, 251301

Sato M., Takada M., Hamana T., Matsubara T., 2011, *ApJ*, **734**, 76

Schmidt F., Rozo E., Dodelson S., Hui L., Sheldon E., 2009, *Physical Review Letters*, **103**, 051301

Schneider P., van Waerbeke L., Kilbinger M., Mellier Y., 2002, *A&A*, **396**, 1

Sellentin E., Heavens A. F., 2017, *MNRAS*, **464**, 4658

Sellentin E., Heymans C., Harnois-Déraps J., 2018, *MNRAS*, **477**, 4879

Shirasaki M., Yoshida N., 2014, *ApJ*, **786**, 43

Shirasaki M., Hamana T., Yoshida N., 2015, *MNRAS*, **453**, 3043

Shirasaki M., Nishimichi T., Li B., Higuchi Y., 2017a, *MNRAS*, **466**, 2402

Shirasaki M., Takada M., Miyatake H., Takahashi R., Hamana T., Nishimichi T., Murata R., 2017b, *MNRAS*, **470**, 3476

Takada M., Hu W., 2013, *Phys. Rev. D*, **87**, 123504

Takada M., Jain B., 2009, *MNRAS*, **395**, 2065

Takahashi R., Sato M., Nishimichi T., Taruya A., Oguri M., 2012, *ApJ*, **761**, 152

Takahashi R., Hamana T., Shirasaki M., Namikawa T., Nishimichi T., Osato K., Shiroyama K., 2017, *ApJ*, **850**, 24

Tanaka M., et al., 2018, *PASJ*, **70**, S9

Taylor A., Joachimi B., Kitching T., 2013, *MNRAS*, **432**, 1928

Tinker J., Kravtsov A. V., Klypin A., Abazajian K., Warren M., Yepes G., Gottlöber S., Holz D. E., 2008, *ApJ*, **688**, 709

Tinker J. L., Robertson B. E., Kravtsov A. V., Klypin A., Warren M. S., Yepes G., Gottlöber S., 2010, *ApJ*, **724**, 878

Troxel M. A., Ishak M., 2015, *Phys. Rep.*, **558**, 1

Troxel M. A., et al., 2018a, *Phys. Rev. D*, **98**, 043528

Troxel M. A., et al., 2018b, *MNRAS*, **479**, 4998

Weinberg D. H., Mortonson M. J., Eisenstein D. J., Hirata C., Riess A. G., Rozo E., 2013, *Phys. Rep.*, **530**, 87

van Uitert E., et al., 2018, *MNRAS*, **476**, 4662

APPENDIX A: FINITE AREA EFFECT OF GAUSSIAN COVARIANCE IN COSMIC SHEAR TOMOGRAPHY

As shown in Sato et al. (2011), the estimator of cosmic shear correlation given by Eq. (9) does not always have a predicted covariance (Eq. 12) even if shear field is assumed to be Gaussian. Eq. (12) will be valid only for wide-area surveys with sky coverage of $\gtrsim 1000$ squared degrees, whereas one need to evaluate the Gaussian covariance from more direct expressions of covariance of estimator itself (see, Eqs.(23)-(25) in Schneider et al. 2002) when the sky coverage is of an order of 100 squared degrees. We here extend the formula in Schneider et al. (2002) by considering the correlation of source galaxies at different redshifts.

Let us return to the definition of the covariance of Eq. (9):

$$\begin{aligned} \text{Cov} [\hat{\xi}_{\pm,ab}(\theta_1), \hat{\xi}_{\pm,cd}(\theta_2)] \\ \equiv \langle (\hat{\xi}_{\pm,ab}(\theta_1) - \xi_{\pm,ab}(\theta_1)) (\hat{\xi}_{\pm,cd}(\theta_2) - \xi_{\pm,cd}(\theta_2)) \rangle. \end{aligned} \quad (\text{A1})$$

In the calculation of Eq. (A1), the four point correlation function of distortion appears. Assuming that the shear field and the source distortion are Gaussian and ignoring the shape noise terms¹³, we can write the four point correlation as the product of the two point function as follows;

$$\begin{aligned} \frac{\langle \epsilon_{\alpha i}^{(a)} \epsilon_{\beta j}^{(b)} \epsilon_{\mu k}^{(c)} \epsilon_{\nu \ell}^{(d)} \rangle}{(2\mathcal{R}^{(a)})(2\mathcal{R}^{(b)})(2\mathcal{R}^{(c)})(2\mathcal{R}^{(d)})} = \langle \gamma_{\alpha i}^{(a)} \gamma_{\beta j}^{(b)} \rangle \langle \gamma_{\mu k}^{(c)} \gamma_{\nu \ell}^{(d)} \rangle \\ + \langle \gamma_{\alpha i}^{(a)} \gamma_{\mu k}^{(c)} \rangle \langle \gamma_{\beta j}^{(b)} \gamma_{\nu \ell}^{(d)} \rangle + \langle \gamma_{\alpha i}^{(a)} \gamma_{\nu \ell}^{(d)} \rangle \langle \gamma_{\beta j}^{(b)} \gamma_{\mu k}^{(c)} \rangle, \end{aligned} \quad (\text{A2})$$

where the above equation is valid for $i \neq j$ and $k \neq \ell$ and Greek letters represent 1 or 2.

From Eq. (A2) and the fact that

$$\epsilon_{\alpha i}^{(a)} \epsilon_{\beta j}^{(b)} + \epsilon_{\alpha i}^{(a)} \epsilon_{\nu \ell}^{(b)} = \epsilon_{1i}^{(a)} \epsilon_{1j}^{(b)} + \epsilon_{2i}^{(a)} \epsilon_{2j}^{(b)}, \quad (\text{A3})$$

$$\begin{aligned} \epsilon_{\alpha i}^{(a)} \epsilon_{\beta j}^{(b)} - \epsilon_{\alpha i}^{(a)} \epsilon_{\nu \ell}^{(b)} = (\epsilon_{1i}^{(a)} \epsilon_{1j}^{(b)} - \epsilon_{2i}^{(a)} \epsilon_{2j}^{(b)}) \cos 4\phi_{ij} \\ + (\epsilon_{1i}^{(a)} \epsilon_{1j}^{(b)} + \epsilon_{2i}^{(a)} \epsilon_{2j}^{(b)}) \sin 4\phi_{ij}, \end{aligned} \quad (\text{A4})$$

¹³ The finite area effect becomes important only for large scales comparable to the size of survey window, making this assumption valid.

where ϕ_{ij} is the polar angle of $\theta_i - \theta_j$, we can express the covariance of Eq. (A1) as follows;

$$\begin{aligned} \text{Cov}_G [\hat{\xi}_{+,ab}(\theta_1), \hat{\xi}_{+,cd}(\theta_2)] &= \frac{1}{N_p^{ab}(\theta_1)N_p^{cd}(\theta_2)} \sum_{ijk\ell} w_i^{(a)} w_j^{(b)} w_k^{(c)} w_\ell^{(d)} \\ &\times \Delta_{\theta_1}(ij)\Delta_{\theta_2}(k\ell) \left\{ \xi_{+,ac}(ik)\xi_{+,bd}(j\ell) + \xi_{+,ad}(i\ell)\xi_{+,bc}(jk) \right. \\ &\quad + \cos [4(\phi_{ik} - \phi_{j\ell})] \xi_{-,ac}(ik)\xi_{-,bd}(j\ell) \\ &\quad \left. + \cos [4(\phi_{i\ell} - \phi_{jk})] \xi_{-,ad}(i\ell)\xi_{-,bc}(jk) \right\} / 2, \end{aligned} \quad (\text{A5})$$

$$\begin{aligned} \text{Cov}_G [\hat{\xi}_{-,ab}(\theta_1), \hat{\xi}_{-,cd}(\theta_2)] &= \frac{1}{N_p^{ab}(\theta_1)N_p^{cd}(\theta_2)} \sum_{ijk\ell} w_i^{(a)} w_j^{(b)} w_k^{(c)} w_\ell^{(d)} \\ &\times \Delta_{\theta_1}(ij)\Delta_{\theta_2}(k\ell) \left\{ \cos [4(\phi_{ij} + \phi_{k\ell} - \phi_{ik} - \phi_{j\ell})] \xi_{-,ac}(ik)\xi_{-,bd}(j\ell) \right. \\ &\quad + \cos [4(\phi_{ij} + \phi_{k\ell} - \phi_{i\ell} - \phi_{jk})] \xi_{-,ad}(i\ell)\xi_{-,bc}(jk) \\ &\quad \left. + \cos [4(\phi_{ij} - \phi_{k\ell})] (\xi_{+,ac}(ik)\xi_{+,bd}(j\ell) + \xi_{+,ad}(i\ell)\xi_{+,bc}(jk)) \right\} / 2, \end{aligned} \quad (\text{A6})$$

$$\begin{aligned} \text{Cov}_G [\hat{\xi}_{+,ab}(\theta_1), \hat{\xi}_{-,cd}(\theta_2)] &= \frac{1}{N_p^{ab}(\theta_1)N_p^{cd}(\theta_2)} \sum_{ijk\ell} w_i^{(a)} w_j^{(b)} w_k^{(c)} w_\ell^{(d)} \\ &\times \Delta_{\theta_1}(ij)\Delta_{\theta_2}(k\ell) \left\{ \cos [4(\phi_{k\ell} - \phi_{j\ell})] \xi_{+,ac}(ik)\xi_{-,bd}(j\ell) \right. \\ &\quad + \cos [4(\phi_{k\ell} - \phi_{ik})] \xi_{-,ac}(ik)\xi_{+,bd}(j\ell) \\ &\quad + \cos [4(\phi_{k\ell} - \phi_{jk})] \xi_{+,ad}(i\ell)\xi_{-,bc}(jk) \\ &\quad \left. + \cos [4(\phi_{k\ell} - \phi_{i\ell})] \xi_{-,ad}(i\ell)\xi_{+,bc}(jk) \right\} / 2, \end{aligned} \quad (\text{A7})$$

where $\xi_{\pm,ab}(ik) = \xi_{\pm,ab}(|\theta_i - \theta_k|)$ and so on.

APPENDIX B: THE FINITE THICKNESS EFFECT IN RAY-TRACING SIMULATIONS

In this appendix, we summarize the effect of finite sampling in comoving distances in multiple-plane ray-tracing simulations. Here we suppose that the ray-tracing simulations have been constructed by N shells of projected mass density at different redshifts. In this case, the integral in Eq. (2) in the ray-tracing simulations should be expressed as

$$\kappa_{\text{sim}}(\theta) = \sum_{i=1}^N \Delta\chi q(\chi_i) \delta^{\text{shell}}(\theta, \chi_i) \quad (\text{B1})$$

$$\delta^{\text{shell}}(\theta, \chi_i) = \frac{1}{\chi_i^2 \Delta\chi} \int_{\chi_i - \Delta\chi/2}^{\chi_i + \Delta\chi/2} d\chi' (\chi')^2 \delta_m(\chi', r(\chi')\theta), \quad (\text{B2})$$

where $\chi_i = (i - 1/2)\Delta\chi$ and we set $N = 38$ and $\Delta\chi = 150 h^{-1}$ Mpc in our case. Under the Born approximation, the lensing power spectrum in the ray-tracing simulation can be computed as the summation of the power spectrum of density shells, denoted as P_m^W . The analytic expression of P_m^W is found in Appendix B in Takahashi et al. (2017). In Takahashi et al. (2017), the authors also provide a simple approximated formula of P_m^W at i -th density shell as

$$P_m^W(k, z(\chi_i)) = \frac{(1 + c_1 k^{-\alpha_1})^{\alpha_1}}{(1 + c_2 k^{-\alpha_2})^{\alpha_2}} P_m(k, z), \quad (\text{B3})$$

with $c_1 = 9.5171 \times 10^{-4}$, $c_2 = 5.1543 \times 10^{-3}$, $\alpha_1 = 1.3063$, $\alpha_2 = 1.1475$, and $\alpha_3 = 0.62793$. Note that the wavenumber k is in unit of $h \text{ Mpc}^{-1}$ and the correction term in Eq. (B3) is independent

of redshift. In addition, the finite resolution in comoving distance in the simulation should be included in the computation of lensing kernel (Eq. 3). We estimate the coarse grained $p(z)$ in the simulation by degrading the original $p(z)$ as shown in Figure 1 with redshift. In summary, we model the finite thickness effect in the lensing power spectrum as

$$P_{\kappa_{\text{sim}},ab}(\ell) = \sum_{i=1}^N \frac{\Delta\chi}{r_{\text{eff},i}^2} q_a(\chi_i) q_b(\chi_i) P_m^W \left(\frac{\ell}{r_{\text{eff},i}}, z(\chi_i) \right), \quad (\text{B4})$$

$$r_{\text{eff},i} = \frac{3}{4} \frac{(r_{2,i}^4 - r_{1,i}^4)}{(r_{2,i}^3 - r_{1,i}^3)}, \quad (\text{B5})$$

where $r_{\text{eff},i}$ is the cone-weighted comoving distance with $r_{2,i} = r(\chi_i + \Delta\chi/2)$ and $r_{1,i} = r(\chi_i - \Delta\chi/2)$ (see also Shirasaki et al. 2015).

APPENDIX C: A HALO MODEL FOR COVARIANCE ESTIMATION OF COSMIC SHEAR

In this appendix, we summarize the formulation based on halo-model approach that used to predict the cosmic shear covariance. We follow the method as in Cooray & Hu (2001), Takada & Jain (2009) and Takada & Hu (2013).

The covariance of cosmic shear tomographic analyses can be decomposed into three terms as shown in Eq. (11). Among these, the Gaussian covariance can be computed with combinations of cosmic shear power spectra. In computing of power spectrum for a given set of tomographic bins (see Eq. 5), we adopt the fitting formula of the non-linear matter power spectrum developed in Takahashi et al. (2012).

On the non-Gaussian covariance, we require a theoretical model of weak lensing trispectrum. Weak lensing trispectrum is defined as (with respect to convergence κ)

$$\langle \bar{\kappa}_a(\ell_1) \bar{\kappa}_b(\ell_2) \bar{\kappa}_c(\ell_3) \bar{\kappa}_d(\ell_4) \rangle \equiv (2\pi)^2 \delta^{(2)}(\ell_{1234}) T_{\kappa,abcd}(\ell_1, \ell_2, \ell_3, \ell_4), \quad (\text{C1})$$

where $\ell_{ij\dots n} = \ell_i + \ell_j + \dots + \ell_n$. Under the Limber approximation, the trispectrum can be computed as

$$\begin{aligned} T_{\kappa,abcd}(\ell_1, \ell_2, \ell_3, \ell_4) &= \int_0^{\chi_H} \frac{d\chi}{r^6(\chi)} q_a(\chi) q_b(\chi) q_c(\chi) q_d(\chi) \\ &\quad \times T_m(\mathbf{k}_1, \mathbf{k}_2, \mathbf{k}_3, \mathbf{k}_4, z(\chi)), \end{aligned} \quad (\text{C2})$$

where $\mathbf{k}_i = \ell_i / \chi$ and T_m represents the trispectrum of matter overdensity field as defined in a similar way to Eq. (C1). Previous studies have shown that the dominant contribution of the non-Gaussian covariance in cosmic shear at relevant scales of $\ell \gtrsim 100$ is given by the so-called one-halo term and the SSC terms (e.g. Sato et al. 2009). The one-halo term arises from the four point correlation among different Fourier modes in single dark matter halos and it is expressed as

$$T_m^{1h}(\mathbf{k}_1, \mathbf{k}_2, \mathbf{k}_3, \mathbf{k}_4, z(\chi)) = \int dM \frac{dn}{dM} \left(\frac{M}{\bar{\rho}_m} \right)^4 \tilde{u}_1 \tilde{u}_2 \tilde{u}_3 \tilde{u}_4, \quad (\text{C3})$$

where dn/dM is the halo mass function, \tilde{u} is the Fourier counterpart of normalized halo density profile (the normalization is set so that the volume integral of the density profile should be unity), and $\tilde{u}_i = \tilde{u}(\mathbf{k}_i, z, M)$. To compute the term of $\tilde{u}(\mathbf{k}_i, z, M)$, we adopt the NFW profile (Navarro et al. 1996) with halo concentration as in Diemer & Kravtsov (2015). For the halo mass function, we adopt

the fitting formula developed in Tinker et al. (2008) throughout this paper.

Another important contributor to the non-Gaussian covariance is the SSC term which includes the four point correlation among super-survey modes. As shown in Takada & Hu (2013), the SSC term can be given by Eqs. (17) and (18). To compute the SSC term, we adopt the halo model of the response of matter power spectrum as follows (Takada & Hu 2013)

$$\frac{\partial P_m(k, z)}{\partial \delta_{\text{bg}}} = I_2^1(k, z) + \left(\frac{68}{21} - \frac{1}{3} \frac{d \ln k^3 [I_1^1(k, z)]^2 P_L(k, z)}{d \ln k} \right) [I_1^1(k, z)]^2 P_L(k, z), \quad (\text{C4})$$

where we use the notation as in Cooray & Hu (2001):

$$I_\mu^\beta(k_1, k_2, \dots, k_\mu) \equiv \int dM \frac{dn}{dM} b_\beta \tilde{u}_1 \tilde{u}_2 \dots \tilde{u}_\mu, \quad (\text{C5})$$

where $b_0 = 1$ and b_1 is set to be the linear halo bias. In this paper, we apply the model of linear halo bias in Tinker et al. (2010).

It is worth noting that the non-Gaussian covariance from the SSC trispectrum requires the computation of the variance in matter density for a given survey window. In this paper, we properly include the mask in real HSC S16A to compute Eq. (18). To do so, we first generate a Gaussian density field on a flat sky by using the linear power spectrum at redshift of interest z . When generating random Gaussian density field, we set the sky coverage to be 20×20 squared degrees and pixel size to be 0.3 arcmin. Then, we paste the survey window subtracted from real HSC S16A onto a squared sky. The survey window of 6 different HSC S16A patches is defined as in Section 3. We confirm that the field of view on a flat sky is large enough to cover the whole survey window in individual HSC S16A fields and the pixel size is sufficiently small to trace a complex geometry of the survey window. After pasting the mask, we compute the variance of Gaussian density field within the survey window. We repeat the above procedures ten times to reduce the scatter in the estimation of $\sigma_W(z)$. The variance estimation has been performed at discrete 20 points in redshifts between $z = 0.001$ and 10 with logarithmic binning of $\Delta \log z = 0.2$. When computing the SSC term in different HSC S16A fields, we interpolate the precomputed 20 data of $\sigma_W(z)$.

APPENDIX D: AN ESTIMATOR OF FIELD VARIATION IN COSMIC SHEAR TWO-POINT CORRELATION FUNCTIONS

Since our mock catalogues of HSC S16A shape preserve a proper positional relationship among six separated patches, those allow us to evaluate the field variation on cosmic shear correlation functions ξ_\pm in HSC S16A.

We here consider the cosmic shear analyses with four different photometric bins as worked in the main text. Suppose that the measurement of ξ_\pm is carried out on individual separated patches, we will characterize a field variation on the measured ξ_\pm among different patches by

$$\Delta \xi_\pm^2(\text{field 1}|\text{field 2}) \equiv [\xi_\pm(\text{field 1}) - \xi_\pm(\text{field 2})]^2 - \text{Var}[\xi_\pm(\text{field 1})] - \text{Var}[\xi_\pm(\text{field 2})], \quad (\text{D1})$$

where $\xi_\pm(\text{field } i)$ represents the observed cosmic shear correlation

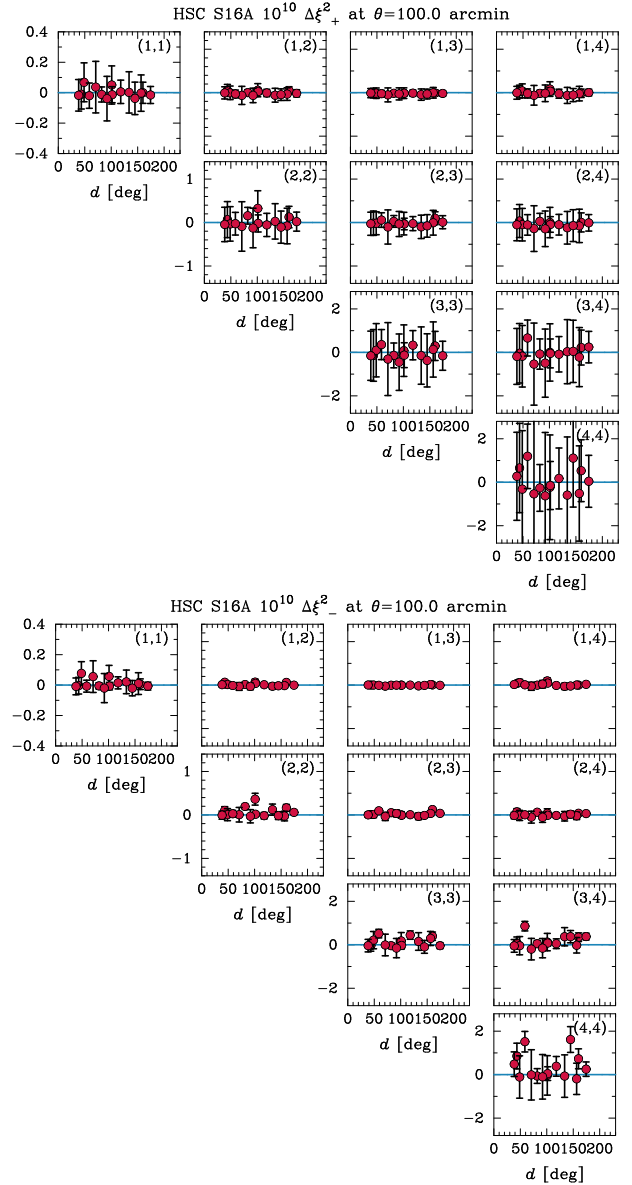


Figure D1. The field variation of ξ_\pm in HSC S16A. We here show the square of difference of ξ_\pm between two separated HSC S16A patches as a function of separation length between two patches d . The estimator is constructed so that we can have a null signal if the measurements of ξ_\pm in two patches are independent each other. The detail of the estimator is found in Eq. (D1). The top panels show the results for ξ_+ , while the bottom is for ξ_- . In both, 10 small panels represents the results with different set of tomographic bins. The legend (1, 2) represents the cosmic shear correlation analysis with first and second tomographic bins, and so on. In each panel, red points are from the HSC S16A shape catalogue and we evaluate error bars from 2268 mock realizations.

function on i -th field, and $\text{Var}[\xi_\pm(\text{field } i)]$ is its variance. The variances in Eq. (D1) can be directly estimated from our mock catalogues. In addition, our mock catalogues enable us to set the statistical uncertainty of Eq. (D1) when we apply the estimator to 2268 realizations of mock catalogues. Note that Eq. (D1) will be evaluated for a given angular separation in ξ_\pm and set of tomographic bins. We construct Eq. (D1) so that we will have a null signal on average ($\langle \Delta \xi_\pm^2(\text{field 1}|\text{field 2}) \rangle = 0$) if the measurement of ξ_\pm is in-

dependent of a choice of survey patches. In this appendix, we study Eq. (D1) as a function of separation length between two fields d .

Figure D1 summarizes the results of Eq. (D1) when we apply to the HSC S16A shape catalogue. In this figure, we work with ξ_{\pm} at 100 arcmin and scale the correlation function by a factor of 10^5 . The top and bottom panels represent the results for ξ_+ and ξ_- , respectively. Each small panel in the top and bottom shows difference in tomographic bins in the analysis. In this figure, the red point is the actual measurement of Eq. (D1) in the HSC S16A data and error bars are estimated from 2268 mock realizations. As seen in the figure, there are no clear trends of field variation of ξ_{\pm} as a function of separation length between separated fields, whereas detailed analyses will be interesting to measure super-sample density fluctuations whose wavelengths are larger than the survey scale in a more direct way (e.g. Li et al. 2014). We leave it for our future work.